Felipe Galvão Rafael Magalhães

A Study on Granular Hopper Flow via Discrete Element Method Computational Simulations

Tese apresentada à Universidade Federal de Minas Gerais como requisito parcial para a obtenção do grau de Doutor em Ciências.

Orientador: Prof. Dr. José Guilherme Moreira

Coorientador: Prof. Dr. Allbens Atman Picardi Faria
Colaborador: Prof. Dr. Hans Jürgen Herrmann

UFMG

Belo Horizonte

2018

À minha esposa e à minha mãe,

Agradecimentos

A Deus, em primeiro lugar, por me permitir chegar até aqui.

Ao Professor José Guilherme, pela paciência de ouvir e ensinar, pelo exemplo como pessoa e como acadêmico.

Ao Professor Allbens pelo seu entusiasmo e seu exemplo de dedicação e prazer na pesquisa.

Ao Professor Hans pela confiança depositada e pela oportunidade de trabalhar em um projeto desafiador ao lado de pessoas incríveis.

Ao tio Roger pela dedicação na leitura do texto e por tornar o processo de revisão mais divertido com piadas a cada e-mail.

Aos professores e funcionários do programa de Pós-Graduação em Física por possibilitar o meu aprendizado e crescimento pessoal e, em especial, ao professor Gerald que respondeu prontamente sempre que o acesso remoto ao Laboratório falhou.

À Carol que partilhou das alegrias e frustrações dessa longa caminhada.

Aos meus pais e à Cleidy sempre dispostos a ajudar em tudo que fosse possível.

Ao Biel, Lu e, meu afilhado, Henrique, pelos momentos de alegria.

A todos os demais familiares pelo apoio e carinho contínuos.

Aos amigos do Sete Verde e da Física em geral, em especial, ao Mangos que dividiu de gabinete até as contas de luz, ao Alex pela presença constante, ao Thiago e ao Clyffe pelas longas pausas para o café.

Aos amigos do NoBonus, em especial, ao Dudu por escutar minhas reclamações.

A todos os amigos do Alto Paranaíba pela amizade insubstituível.

I thank the Comphys Group at ETH-Zürich for the hospitality. Especially, I thank Alessandro for the help with the code and for, along with Gautam, making work not so boring. Agradeço ao Vítor Hugo e a Helen pela hospitalidade quando faltou chave do apartamento, pela companhia nas viagens, pelas longas conversas no Fine Choice e,

sobretudo, pela sincera amizade.

À CAPES que financiou a bolsa no Brasil e ao CNPq que concedeu a bolsa na modalidade Sanduíche no Exterior.

Resumo

O estudo do fluxo de grãos tridimensionais esféricos através de funis cônicos pelo Método de Elementos Discretos revelou aspectos importantes da estrutura e dinâmica da descarga de matéria granular. As quantidades analisadas foram a velocidade média dos grãos, além da série temporal e da distribuição das forças sobre a parede do funil. Foi observado uma diferença entre as velocidades dos grãos próximos à parede do funil e ao longo do seu eixo central. Propusemos um novo índice dependente da coordenada radial definido como a razão dos perfis de velocidade e ele foi capaz de representar essa diferença e, portanto, representando o comportamento do escoamento de forma detalhada. Chamado de índice de fluxo de massa local, seu valor varia entre 0,50 e 0,85, dependendo do diâmetro do orifício, até próximo da unidade, ao longo da parede do funil. Este comportamento indica que grãos próximos da superfície superior tem velocidade homogênea para uma mesma distância do vértice do cone, diferentemente do que ocorre próximo da abertura. A série temporal das forças exercidas pelo material granular sobre a parede do funil revelou flutuações compatíveis com ruídos correlacionados tipo $1/f^{\alpha}$. Observou-se que o expoente α é dependente da distância do orifício, com valores nulos próximos ao orifício e alcançando um platô em torno de $\alpha = 1{,}8$ para distâncias maiores. Este valor é compatível com o reportado na literatura em regimes de fluxo de funil, com presença de zonas de estagnação, ausentes no presente trabalho. As funções densidade de probabilidade para as forças entre os grãos e a parede em diferentes distâncias da saída apresentaram comportamento gaussiano ou caudas exponenciais. A distribuição gaussiana ocorreu para uma longa faixa de distâncias intermediárias e é indicação de homogeneidade na estrutura dos grãos, ou seja, grãos em empacotamento denso. Enquanto isso, em regiões imediatamente acima do orifício ou próximas à superfície livre do material granular a distribuição apresentou caudas exponenciais, indicando uma maior presença de forças acima da média, causadas tipicamente pela presença de cadeias de força que causam uma estrutura de arcos e vãos, e um empacotamento dilatado. Concluímos então que a ausência de zonas de estagnação observada nos perfis de velocidade é contrastada por valores intermediários do índice de fluxo de massa local e por estatísticas das forças exercidas sobre o funil compatíveis com a presença de estruturas organizadas de grãos que se movem ao longo do funil, um possível precursor do regime de fluxo de funil.

Palavras-chave: Física de Matéria Granular, Física Computacional, Dinâmica Molecular

Abstract

The study of the flow of three-dimensional spherical grains through conical hoppers via Discrete Element Method revealed important aspects of the structure and dynamics of the discharge of granular matter. The characteristics analyzed were the average velocity of the grains, as well as the time series and the distribution of forces exerted on the hopper. It was observed that a difference exists between the velocity profiles close to the wall of the hopper and its central axis. We proposed a new index in function of the radial coordinate defined as the ratio between these two profiles and it was effective in representing this difference and, consequently, representing the flow behavior in detail. It was named local mass flow index and its values varied between 0.5 and 0.85, depending on the orifice diameter, rising to values close to unit up along the hopper wall. This behavior indicates that grains close to the top surface have homogeneous velocity distribution at the same distance from the cone vertex, unlike what occurs close to the orifice. The time series of the forces exerted by the granular material on the wall of the hopper revealed fluctuations compatible with correlated $1/f^{\alpha}$ noise. It was observed that exponent α is dependent on the distance from the orifice, with null values close to the outlet and a plateau around $\alpha = 1.8$ being reached for larger distances. This value is consistent with literature reported for funnel flow regime, where stagnation zones are present, which were not observed in this work. The probability density function for the forces between the grains and the wall at various distances from the outlet presented one of two behaviors: Gaussian-like distribution or exponential tails. The Gaussian distribution occurred for a wide range of intermediate distances and it is an indication of homogeneity in the structure of the grains, *i.e.*, grains in dense packing. On the other hand, functions at regions immediately above the orifice or close to the free surface of the granular material presented exponential tails, indicating the presence of more forces above average. That is caused, typically, by the presence of force chains in a structure of arches and vaults, and a more dilated packing. We conclude, then, that the absence of stagnation zones observed in the velocity profiles is contrasted with intermediate values for the local mass flow index and by statistics of the forces on the wall compatible with the presence of organized structures that move along the hopper, and configuring as a possible precursor of funnel flow regime.

Keywords: Physics of Granular Matter, Computational Physics, Molecular Dynamics

Summary

1 Introduction

Granular matter, the subject of this thesis, is present in almost all human activities, from agriculture to mining and pharmaceutical industries. It has attracted great interest from physicists and engineers due to its applicability and rich phenomenology [1, 2, 3, 4, 5, 6, 7, 8].

Granular physics is understood as the description of the dynamics of a collection of solids, where the interaction between objects plays the main role, that is, the overall behavior is not influenced by the thermal agitation of the interstitial fluid. The origin of the materials can vary greatly, including seeds, coal lumps, powders in pharmaceutical and cosmetic industry and even icy particles in the rings of Saturn are part of this long list. We discuss further on what is necessary for a material to be considered granular in the following chapter.

The economical relevance of granular materials is contrasted by the paucity of technological improvements employed even today. As discussed by Duran [5], granulars are regarded as the second class of materials among human priorities, the first being water. He states that a total of 10% of the energy produced in the planet is employed in processing grains and aggregates. The annual production of granular materials was estimated to be over 10 billion tons and coal was responsible for over a third of that in the year 2000, the time of publication of the book. According to the International Energy Agency, the global production of coal alone has been estimated to have risen over 7 billion tons in the year of 2016 [9]. Nevertheless, primitive techniques dating back to the 19^{th} century are still currently in use, such as hammering hopper walls in order to unblock an interrupted granular discharge.

Many unexpected effects emerge from the inter-grain interaction in a bulk of solids and most of them are still not well understood. For instance, at high density, particulate matter resists shear like a solid, nevertheless, it flows at lower densities. Even so, the flow of granular material is different from that of liquids, for instance, hourglasses work

based on the fact that the flow ratio of the sand through the orifice does not depend on the height of the pile of grains on top. Moreover, in the last decades, with the increasing computational performance of codes based on the Discrete Element Method (DEM), there has been a new surge of interest in the subject with the possibility of simulating large systems at the scale of real experiments.

In this thesis, we study the flow of dry spherical grains through a conical hopper via Discrete Element Method simulations in three dimensions. Efforts have been made to understand the multitude of features presented by the flow of granular materials through a bottleneck such as clogging [10, 11, 12, 13, 14], density fluctuations [15], segregation [14, 16], strong fluctuations on the forces acting on silo walls [17, 18, 19, 20] and the collapse of silos during discharge [21]. An important property of granular discharges is that two distinct flow regimes can be observed — mass flow and funnel flow —, depending on the material properties of the grains and walls, and mostly on the hopper geometry (grain-wall friction, opening angle, orifice size, among others) [22, 23, 24, 25]. Therefore, the better understanding of these phenomena, particularly the influence of the design of silos, can impact directly the industry of bulk solids.

The flow regime classification is often based on visualization of the steady state. Through the decades it has evolved from the mere visual observation of stagnation zones on experiments [25] to the time averaged velocity spatial distributions, either by color scaled two-dimensional fields or profile curves along a certain linear path. Velocity profiles, particularly, are widely applied in the field of granular discharge flow[26, 27, 28, 29]. The funnel flow regime is then recognized by the presence of stagnation zones in the velocity fields or a large difference between the velocity in the central region and that close to the walls, see Figure 1. In order to quantify this difference, an index has been defined[22, 30], the Mass Flow Index (I_{MF}), corresponding to the ratio of the average particle velocity next to the hopper wall, v_{w}, to the average particle velocity at the hopper centerline, v_{c}, that is, $I_{\mathrm{MF}} = v_{\mathrm{w}}/v_{\mathrm{c}}$. In the literature, the convention is that if $I_{\mathrm{MF}} < 0.3$ the regime is funnel flow, and mass flow otherwise [22, 23, 30].

Ketterhagen *et al.* [30] used this index to create design charts for wedge shaped and conical hoppers, that is, they measured I_{MF} from simulations for different pairs of grain-wall friction and hopper wall angle and built a phase diagram to serve as a guideline for the designing of hoppers. For this, they averaged v_{w} and v_{c} over a large region spanning along the hopper walls and the centerline, respectively.

The velocity dependence on the vertical coordinate is usually assumed to be equal

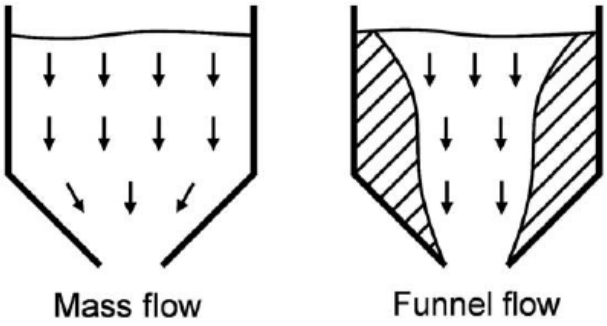

Figure 1: Flow regimes are represented schematically. (Left) mass flow; (Right) funnel flow. Figure adapted from Reference [30].

to that of an incompressible fluid[31, 22]. In the case of an incompressible fluid flowing through a conical hopper with an angle Θ with the horizontal plane, we can easily obtain the velocity dependence on the vertical coordinate. The volume flow rate is defined as $Q = Av$, where A is the cross sectional area and v is the velocity. The flow rate must be constant along the direction of the flow, provided that the density is homogeneous for an incompressible fluid. Thus, consider a point at height z_o on the hopper opening, where $Q_o = A_o v_o$, and an arbitrary point at height z in the hopper, where $Q = Av$, then, due to mass conservation,

$$\frac{Q}{Q_o} = \frac{Av}{A_o v_o} = \frac{\pi \left(z \tan \Theta\right)^2 v}{\pi \left(z_o \tan \Theta\right)^2 v_o} = 1$$

and, from that,

$$v = \left(\frac{z}{z_o}\right)^{-2} v_o. \tag{1.1}$$

Therefore, for an incompressible fluid, the velocity decays as a power law along z with exponent -2. However, if Equation 1.1 holds for a granular discharge, the procedure used by Ketterhagen *et al.* [30] may lead to an I_{MF} value that is highly sensitive on position and size of the averaging region. This would cause their design charts to be applicable only if the same specifications were used. In fact, González-Montellano *et al.* [26] calculated, among other quantities, the ratio of the wall and center velocities, but averaging them over small regions at a few different heights along a square cross-section silo with a hopper-bottom that has square geometry. Although the ratio was approximately equal to one all along the vertical silo, they observed that inside the hopper the ratio largely fluctuated reaching values below 0.3 at some points, even though they consider the discharge to be in the mass flow regime. In their analysis the I_{MF} played a smaller role and they did not consider it a profile, but only an quantifier of the slope of the horizontal velocity profile.

Granular flow may differ from incompressible fluids as there are voids and, therefore, density heterogeneities occur, even though each grain is roughly incompressible by itself.

In fact, one can expect that a larger density would be observed at positions farther from the hopper outlet, where the velocity is smaller and the grains are in a densely packed structure, as compared to regions closer to the orifice, where the velocity is larger and grains are looser. As shown by Sielamowicz and Czech[32] in experiments discharging amaranth seeds through a two dimensional hopper, the assumption of an incompressible fluid is not always valid. They found discrepancies from the 2D equivalent to Equation 1.1, especially, close to the outlet. Additionally, their flow regime was closer to funnel flow as there was the formation of a channel of flowing grains in the central region of the hopper, while the grains close to the walls of the hopper were stagnant. Also mixed flows may occur, where an upper section of the hopper is in mass flow regime whereas the bottom section is in funnel flow regime.

In order to contribute to this discussion, we present in this Thesis the velocity fields and the velocity radial profiles for the simulation of the discharge of spherical grains in a conical hopper. The velocity fields calculated are similar to those found in the literature. The velocity profiles along the centerline and along the walls of a conical hopper behave roughly as power laws. Nevertheless, there are some differences between v_{c} and v_{w} profiles that carry information about the flow regime. We propose the Local Mass Flow Index profile and its analysis as a method capable of extracting that information in a clearer way. We follow the basic idea presented by González-Montellano *et al.* [26], where the I_{MF} is calculated in small areas, however, we consider it a profile in function of the distance from the hopper vertex. This method should be applicable independently of the validity of any assumption about velocity radial dependence. Furthermore, we believe that the Local Mass Flow Index analysis may lead to a more precise definition of the flow regime boundaries.

Complementarily, we study the distributions and correlations of forces acting on the walls of the hopper during discharge. The forces exerted on the walls of a hopper by flowing grains is a matter of crucial importance for the solids handling in many industrial activities and poor knowledge of their behavior have been the cause of many disasters in industrial plants over time. Unexpectedly large forces may be exerted by granular materials during discharges causing silos to collapse and entire industrial plants to crumble, as we discuss in Section 2.3. We observe that different regions in the hopper present different probability density functions of the forces on the walls, with forces much larger than average being more likely to occur close to the outlet (heavy tails) and more compact distributions found for intermediate positions along the hopper walls. Additionally, the time series of such forces are more correlated on regions further up the hopper than close to the orifice, where

the force signals are close to white noise.

We discuss more of the phenomenology of granular materials in Chapter 2. Some of the many computational methods for the simulation of grains are reviewed in Chapter 3, and, subsequently, in Chapter 4, we present the details of the method we have used for our code. The analysis of the flow patterns based on velocity field and velocity profiles is discussed in Chapter 5, followed by the analyses of the distributions and fluctuations of the force exerted by the grains on the wall of a hopper in Chapter 6. We present our conclusions and perspectives in Chapter 7.

2 Granular Matter

In this chapter we shall present a fraction of the rich phenomenology of granular physics. It follows the spirit of reviewing papers [1, 2, 3]. Firstly, we discuss the criteria for a collection of solids to be considered granular matter in Section 2.1. In the following section, Section 2.2, we discuss the difficulties of mixing grains of varied shapes or sizes. In sections 2.3 and 2.4, we discuss the effects of energy loss due to the inelastic collisions and the peculiar spatial structure of the network of contact forces in dense packings, respectively.

2.1 What is and What is Not

What can be considered granular matter is a good question to start [5]. One can make a pile of salt in the kitchen to resemble the pile of coal lumps in a mining site, even though the typical sizes of the involved particles are respectively $0.1mm$ and $10cm$, that is, at least four orders of magnitude apart. In fact, the size of the objects that can be regarded as granular matter can be even larger than that, including icebergs and the asteroid belt of the solar system. There is, however, a lower threshold of size of particles for them to be governed by granular physics. Actually, size plays an indirect role, as the major concern is the scales of the kinetic and thermal energies. In granular physics the dynamics is dominated by the relative motion of the particles, and their thermal agitation or that of the interstitial media must not influence their movement. Therefore, the scale of particle sizes is indirect, as the effective criterion is that the kinetic energy should be sufficiently larger than the thermal energy. That typically happens for particle diameters of the order of tenths or hundreds of microns. The reason for the difficulties in obtaining a hydrodynamic description of granular materials is then evident, as one cannot dissociate the movement of the bulk from the movement of the particles therein.

2.2 Mixing versus Segregation

The absence of thermal agitation is relevant, for instance, in the discussion of mixing grains of different sizes, shapes or materials. That is because there is no effect similar to Brownian motion in granular dynamics, which is responsible for mixing in liquids. It is not only difficult to get a homogeneous mixture of grains, but intuitive approaches often lead to the exact opposite effect: segregation.

The phenomenon of segregation is a major problem in handling of granular materials in industry. In pharmaceuticals for instance, segregation can lead to irregular dosages in pills [7]. In other situations, the contact between different particles may enhance or enable a chemical reaction and, therefore, mixing is necessary. Nevertheless, typical attempts to mix grains, such as shaking a can of varied nuts will actually result in a separation of the different types of nuts, with the larger on top. This seems contrary to the intuitive concept in fluid dynamics of buoyancy, where the lighter of two immiscible fluids floats over the heavier.

The rising of large grains under vibration came to be known as the Brazil nut effect, named after the very example discussed above, as in varied nuts cans the Brazil nut is usually the largest. It is also a good example of the difficulties in handling granular matter, as the mechanism behind this effect has been subject of a long debate. The effect was first understood as a result of the higher mobility of the smaller particles [33, 34]. This kinetic argument contrasted with a study published almost simultaneously [35], where the authors argued the main mechanism at play is the rolling up of the large grain over the smaller ones. This was based on the effect of the friction coefficient, as for small values of this parameter the effect was not observed. Additionally, a geometrical explanation was developed [36], the argument being that the smaller particles would eventually fill the voids below the larger ones as the container is vertically shaken. Later, the role of convection was argued to be fundamental to the occurrence of the upward motion of the largest particles [37, 38, 39]. And, as if the scenario was not complex enough, it was proposed that a "reverse Brazil nut effect" would occur for certain combinations of the densities of the large particle and the smaller ones [40]. In the reverse effect, the largest particle, rather than rise above the small ones, will sink below them. In summary, it seems that many factors influence the Brazil nut effect. Each experimental setup or theoretical assumption seems to focus on different aspects of this complex subject and this is why it is still an active field of research. We recommend reference [41] for a thorough review of the subject.

The Brazil nut effect is not the only example of segregation in granular materials. Stratification [42, 43], segregation in the arches of a clogging outlet [14] and many other phenomena make the mixing of grains a surprisingly complex problem of academic and industrial interest.

2.3 Inelasticity

The inelastic character of interactions between colliding grains has an important influence in the singular behavior of flowing granular matter. As result of such loss of energy, there is no separation of the motion at the grain scale from the hydrodynamic motion of the bulk even for fast granular flows. Additionally, the viscosity depends on the velocity of the flow, and therefore granular materials flow as a non-Newtonian fluid.

Many phenomena in granular flow are due to energy loss in collisions. The flow is prone to heterogeneities, as grains entering a region of higher density are more likely to lose energy and aggregate. Therefore clogs are formed. The bigger the clog the more grains aggregate. Many effects arise from this such as the density waves in pipe flow, silo-quakes in emptying silos and the clogging of outlets [1, 44, 12, 13].

The term silo-quake was based on both the similarities of statical properties and destructive effects of this phenomenon and seismic earthquakes. It is a self-driven instability that occurs due to fluctuations in density and, therefore, in pressure, in granular matter flowing through a pipe or silo so that waves of arbitrarily large wavelength are produced, which can cause entire buildings to collapse. The statistics of shocks between grains and wall resemble those known for earthquakes, showing power law frequency distribution and $1/f$ power spectra [45, 44]. Similar noise properties are shown by the actual sound of granular flows [45, 46]. Similar power spectra are observed in the time series of the forces exerted by grains flowing through a hopper as discussed in reference [15, 17] and in Section 6.1.

The instability of density heterogeneities as we discussed may lead to formation of clogs in flowing granular matter. A particularly important clogging event type is that which leads to an obstruction of the outlet. In such situations another facet of granular dynamics plays an important role: the force networks, that we shall discuss in the next Section, before returning to clogging in Section 2.5.

2.4 Force Networks

Dense granular packings present very different behaviors for different setup histories. These differences are intimately related to the force chains and force networks formed in the packing. Many properties affect the structure of these networks, such as, the coefficient of friction and the shape of the grains. However, the procedure to form the packing is a leading feature, as we shall show throughout this Section.

The importance of force networks was highlighted over a century ago by H. A. Janssen [47, 48]. He performed a pioneering experiment that came to enlighten the interactions between the walls of a silo and the grains inside it. Although some assumptions in the theoretical calculations were inaccurate [1], his observations and qualitative description were correct and defined what came to be known as Janssen Effect. He observed that for a silo filled above a certain height, pouring more grains or placing an overload influences very little the pressure measured at the bottom, as shown in Figure 2. This saturation contradicts the behavior observed in fluids, where the pressure is linearly proportional to the height of the fluid column. The effect is, however, explained by the presence of force chains that extend from one side of the silo to the other, forming arches that transfer the weight of the grains above them to the walls of the silo.

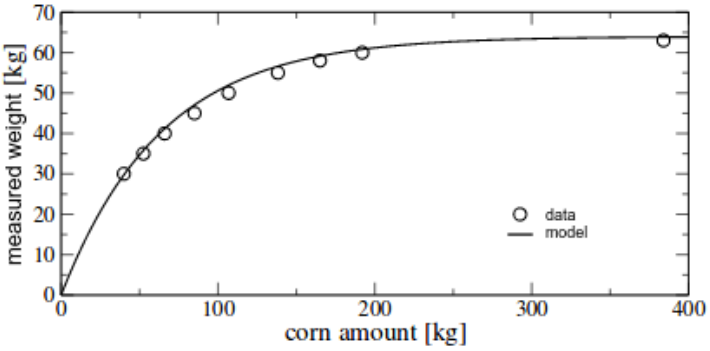

Figure 2: Bottom pressure —measured as weight on the bottom plate —as function of corn amount. Figure adapted from Reference [48].

In a pile of grains built from a localized-source, *i.e.*, all grains are released from the same horizontal position, an effect known as the sandpile pressure dip effect shows itself as an interesting example of the force network phenomenology [49, 50, 51]. The pressure

[1] The inaccuracies in the arguments in the original paper are discussed in details in its translation [48]. In summary the three most important of such inaccuracies or approximations are the assumption of full mobilization of friction at the walls; the vertical and horizontal stresses are introduced as principal stresses; and a uniform distribution of stresses is assumed along any slice of the silo.

exerted by the pile on the substrate has a minimum aligned with the position of the grain source and, therefore, the peak of the pile, see Figure 3(a). The minimum disappears when the pile is built by a rain procedure, by which the grains are released after passing through a sieve and are deposited on random horizontal positions, see Figure 3(b). The pressure spatial distribution on the substrate is different because the force networks that carry down the weight of the grains are different in each case. For the localized-source procedure the force chains follow the slope of the pile itself, forming complete arches under the peak, as seen in Figure 4. These arches are responsible for redirecting the pressure out of the center of the pile. On the other hand, a pile constructed by the rain procedure present force chains that are significantly less ordered, and thus the dip under the heap effect is weaker.

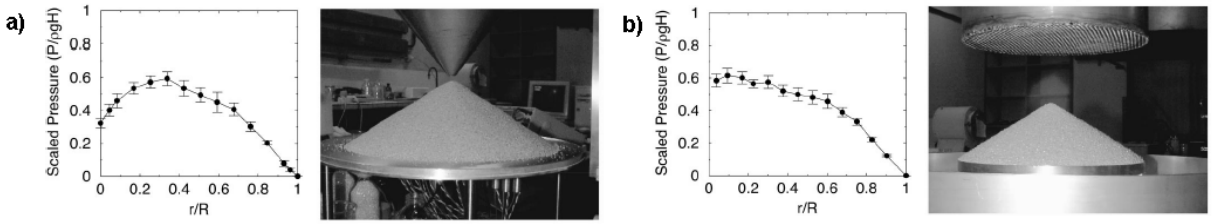

Figure 3: Pressure profile for conical piles. Pressure is measured by a capacitive sensor positioned on the base plate and calibrated against the hydrostatic pressure of a water column. Horizontal axes are presented as the ratio r/R, the distance from the center of the base plate, r, divided by its radius, R. (a) Localized-source procedure; (b) raining procedure. Figure adapted from Reference [50].

An analogous effect was observed by manipulating the force network before probing the pressure response of a granular bed by a localized overload [51]. The granular bed is prepared by simple shearing, which causes anisotropies in the force network and it was observed that, as a result, the stress response at the bottom for different pressure applied to the top of the material is skewed. Therefore, the response function can be used as part of systematic approaches to probe stress-strain history and constitutive parameters of the material.

Several of the phenomena observed in granular physics are only understood considering the role played by force networks. In the following section we discuss a few of the many such instances.

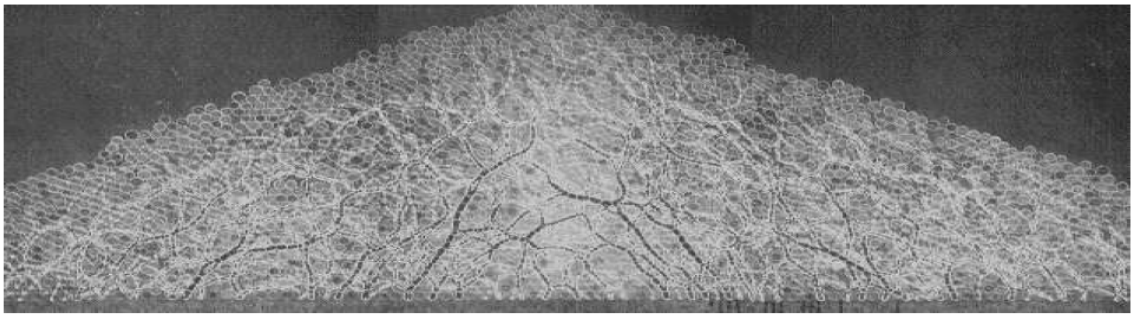

Figure 4: Pile of photoelastic discs showing force chains. Figure adapted from Reference [52].

2.5 Jamming, Clogging and Dilatancy

The term "jamming" has been traditionally used to define the static state of granular matter under stress, or shear, where the rigidity increases with increasing density. Liu and Nagel [53] proposed a phase diagram for jamming and included not only grains but colloids, foams and glasses among the systems capable of transitioning to a jammed phase. An interesting difference between the jammed phase and solid phase, apart from the presence of a crystalline structure only in the latter, is that the rigidity of the first is sensitive to the direction of the applied stress and, for that reason, is also called fragile matter [54]. A sand pile, for instance, is stable when subjected to its own weight, but will crumble under horizontal vibrations.

The description "jammed" has also been applied to the state of grains whose flow is interrupted by the formation of an arch (or dome in three dimensions) above an outlet. There has been some controversy in the nomenclature of this state and in recent works there has been a tendency towards the term *clogging* in order to dissociate these events from the traditional jammed state. Although, nucleation of high density regions is responsible for slowing down the flow, as discussed in Section 2.3, the arch of grains that span across the outlet is the one responsible for sustaining the weight of the grains above, preventing the flow. There have been many papers dedicated to understanding the clogging of an outlet, most of them focusing on the shape of the arch and on the probability of such an event occuring [55, 11, 14, 12, 13, 56, 57]. The existence of a phase transition from an always-flowing phase to an incidentally-clogging phase has been disputed in the last few years. An experimental work, performed by Janda *et al.* [11] obtained the probability of an arch to block outlets of varied widths. Their data showed good agreement with the analytical predictions of two opposite hypotheses: a phase transition between clogging and never-clogging states and that where the clogging has non-zero probability

for any outlet width, *i.e.*, arches will eventually block the flow no matter how large the outlet. They argued the latter to be correct in two dimensions as it was corroborated by a stochastic simplified model of the formation of the arch presented in the same paper. This result was contradicted by simulations of discharges in a pile of grains [12, 13], where a critical behavior was observed for the phase transition. For this system, discharges become catastrophic, that is, no clogging occurs and the pile is split in two, for outlet widths larger than a certain finite value.

Dilatancy is another important example of counter-intuitive behavior of granular materials and also related to the structure of the force chains. It can be observed when we step on wet sand on the beach and it seems to dry out. Naively, one could expect that under the pressure applied by our foot the sand beneath it would contract and water would, effectively, rise above the sand. However, the grains align themselves under stress in a more organized structure, creating force chains to support the pressure in response. The new structure of the material houses more voids where water is caught. This effect was coined by Reynolds [58] and exemplified by him with an experiment we can easily recreate. Take a rubber balloon filled with grains and attach a straw to its opening. Fill the apparatus with water until its level is visible at the straw, see Figure 5a. If we squeeze the balloon, the water level will fall, Figure 5b, just as the sand at the beach gets dry under our weight. Dilatancy play a important role in soil mechanics, where the precondition of the soils may influence its resistance to shear, and therefore it has to be considered when building tunnels and piles on compressed soils.

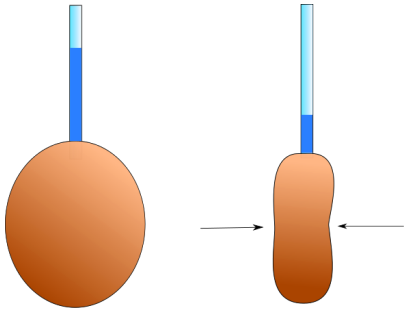

Figure 5: Dilatancy experiment is represented schematically. Before (a) and after (b) external pressure is applied. Water level lowers, because granular material is dilated. Figure reproduced from [59].

Granular matter presents an extensive phenomenology and what we have discussed throughout this chapter is just a small fraction. There is a large number of open questions in the field and the subject has not received the attention it deserves until recently. Since a few decades ago a new interest has risen around granular materials mainly because of

the advances in reliable computer simulations that enable new insights into the dynamics of grains. In the next chapter, we discuss the most important numerical approaches, their advantages and limitations.

3 Methods of Computer Simulations of Granular Materials

> "Who could ever calculate the path of a molecule? How do we know that the creations of worlds are not determined by falling grains of sand?"
>
> Victor Hugo, Les Miserables

Granular materials have proven to be a capricious subject to be handled either experimentally or analytically. The pursuit for "granular thermodynamics" is still on [60], while experimental assessment of some microscopic characteristics of the material is difficult or sometimes impossible. It is in this context that the numerical approach flourishes as the main tool for scientists investigating grain packings and flows. The complete freedom in the choice of parameters, the easy access to any variable in the system and the low cost are just a few of the advantages of such an approach. Of course, there are disadvantages, for instance, the approximations required for the adaptation of a real world problem into the limitations of computer memory and numerical results lack the generality which can only be provided by an analytical approach. However, it has been shown throughout the last decades that computer simulations are capable of representing granular systems well enough to solve several queries, both academic and applied.

In this chapter we shall discuss the main numerical methods employed in computer simulation of granular materials. Our main references in writing this chapter was the book by Pöschel and Schwager [61] and the Master Thesis and Doctorate Thesis by Caio F M Magalhães [62, 63]. In the first section we discuss the idea behind the Molecular Dynamics or Discrete Element Method (DEM), which we have chosen to apply in our investigations. Section 3.2 is dedicated to the Event Driven Method, very efficient for low density granular systems. The Monte Carlo Method is discussed in Section 3.3. Finally,

Section 3.4 is a presentation of the broad class of methods based on Cellular Automata.

3.1 Molecular Dynamics and DEM

The first attempt at simulating numerically the time-dependent dynamics of many-body systems was motivated by the behavior of molecules in bulk and therefore it was suitably named Molecular Dynamics (MD). Although the interaction between a pair of molecules could be well described analytically in the middle of the 1950s, the description of a system composed of many molecules was, and still is, a challenging subject. In the words of Alder and Wainwright [64]:

> One of the great difficulties in the present day theoretical attempts to describe physical and chemical systems is the inadequate mathematical apparatus which has been available to solve the many-body problem. Thus, although the properties of an isolated molecule are well established and the elementary processes which occur when two such molecules interact are described by well-known laws the behavior of systems of many interacting molecules cannot, in general, be dealt with theoretically in an exact way. Even a three-particle system presents great analytical difficulty. Since these difficulties are not conceptual but mathematical, high-speed computers are well suited to deal with them.

It was at this time that the new-found power of numerical analysis through computer simulations inspired the development of the MD methods that opened a new research field. The MD method designed to simulate molecules was soon implemented with little modification to macroscopic particles systems in engineering applications. In this context, MD was coined Discrete Element Method (DEM) by Cundall in 1971 [65] after having some complementary features added in the model, such as the rotational degrees of freedom. Since then, a long list of improvements and variations of what is understood as DEM has been created. The basic principles are maintained:

- Short range pairwise interaction between particles;
- Time evolution given by integration of the equations of motion for each particle.

In the context of granular materials, the interaction is usually given by a force law obtained from the experimental or theoretical analysis of the collision of a pair of grains.

DEM is also suitable for applications in combination with other methods such as Fluid Dynamics [66, 67, 68].

One of the advantages of the DEM is the wide range of experimental situations to which it has successfully been applied. It can be modified to replicate different material properties, such as cohesion, by simply changing the force law. Also with the DEM many features that are experimentally hard to obtain —such as the force network that require sophisticated techniques from experimentalists —are, however, readily available in the computational approach. The DEM is possibly the numerical method that can most easily be set up to represent experiments.

The major drawback of the method is the computationally expensive calculations required by the integration of the equations of motion. These calculations occur even if there is no contact between grains, which can be a common situation in gases. In these cases the more appropriate method would be the Event Driven method, an adaptation of the DEM, discussed in the next section.

3.2 Event Driven

The efficiency of the Molecular Dynamics method can be improved for dilute granular systems. The improved method is known as Event Driven Molecular Dynamics or simply Event Driven method (ED). As the name suggests, in this method computations occur only during the event of a collision, that is, the intervals between collisions are not simulated at regular time steps as in MD, therefore the efficiency increases. The collisions between particles are considered as instantaneous and governed by a collision law derived from momentum and energy transfer relations and influenced by the coefficient of restitution. The collision laws may vary relatively to the problem one needs to simulate. The law estimates predictions of the linear and angular velocities of the grains after the collision based on the ballistic trajectories of the grains and their velocities before the collision. The main parameter is therefore the coefficient of restitution, which is defined by the ratio between the pre-collision and post-collision velocities. After a collision, the next event is predicted by checking the crossing of the ballistic trajectories of the grains.

The advantages of the ED method are obvious, as they are the very basis of the modifications to the original Molecular Dynamics methods, namely the increase in computational efficiency. Also, some traditional disadvantages have been circumvented in more modern approaches such as including non-instantaneous collisions via soft particles

interactions in ED methods [69]. However, the method still presents an important drawback that limits its applications: the limitation to pairwise contacts, preventing its use to simulate dense granular systems where events where three or more grains are in contact simultaneously occurs frequently. In summary, the Event Driven Molecular Dynamics method is highly recommended for the simulation of granular gases, but is not applicable to granular packings or dense granular flows such as the one we study in this thesis.

3.3 Monte Carlo

The traditional Molecular Dynamics methods, sometimes referred to as time driven Molecular Dynamics, and their adaptation, the Event Driven methods, are all based on the microscopic dynamics of the grains. There are other methods in which the chronology and dynamics of the micro-interactions are completely abandoned. That is the case of the Monte Carlo based methods, also known as Direct Simulation Monte Carlo(DSMC) [70]. This method is based on kinetic theory arguments and departs from the idea of computing individual trajectories of grains, in such a way that only the statistical properties of the granular material can be extracted, but not its dynamics. The general premise of Monte Carlo method is maintained in the DSMC, that is, the random sampling of the system configuration based on the hypothesis of the system being in a stationary state.

The formal definition of the Monte Carlo method includes the knowledge of the probability density function of the states of the system, which is, in general, impossible to obtain. In most cases, it is necessary to resort to physical arguments in order to sample the system configurations. We suggest Chapter 4 from the book by Pöschel and Schwager [61] for a practical approach on the method and Appendix B from the master thesis by Magalhães [62] (in portuguese) for a theoretical overview.

The DSMC methods are capable of recreating many experimentally observed phenomena. For example, the Brazil-nut Effect [62, 33] and clustering in granular gases [61] were successfully replicated. The computational efficiency of this method is its main advantage, even though it results in the absence of information about the evolution of the system over time. The method is mainly useful for studies where the interest lies exclusively in the statistical properties of the granular material.

3.4 Cellular Automata

Cellular automata are computational models defined over a lattice and subjected to local rules that govern the entire dynamics of these systems. The rules define the state for each site in the next time step simply by the state of its surrounding sites. Therefore, once the system is initialized, it will evolve, changing the state of each site (cell) automatically. Although cellular automata are a subject of their own, there have been successful applications of this concept to simulate granular systems. It has also been the inspiration for other bottom-to-top methods, where only the essential properties of the material are considered for a simplified model of the system.

The field of cellular automata is rich and not confined to applications in physics, as it is also applied in investigations in sociology, biology and economics, for instance [71, 72, 73]. The application of cellular automata to granular materials was negligible until the publication of the works by Bak, Tang, and Wiesenfeld [74], where it was demonstrated that the piling of a heap could present Self-Organize Criticality. Although some applications have raised controversy, it has become a common tool in the literature in the past three decades. Usually, two states are considered for each site: empty or occupied by a grain. The rule, therefore, dictates the movement of the grains, that is, one site becomes empty, while another becomes occupied.

In general, the rules of a cellular automata simulation is set up to pursue a specific query and cannot be applied in any other context. Also, the results are only qualitatively comparable to experiments. This approach is therefore useful to demonstrate the basic properties necessary for a phenomenon to occur or to motivate the investigation of a new phenomenon by another method. However, the cellular automata method is very useful for physical insights and for its computational efficiency. A setup may be restricted to a single investigation and, typically, it would provide only qualitative results.

4 Our Model

In this chapter, we discuss in detail the numerical model utilized to simulate the flow of dry grains through a hopper. We have chosen the Discrete Element Method, as discussed in Chapter 3, that is the most adequate tool to simulate dense flows in which grains present multiple long lasting contacts.

The code was written following mainly the book by Pöschel and Schwager [61]. The algorithm can be understood through the flowchart presented in Figure 6. We first initialize the system, assigning values for the coordinates, their derivatives and parameters, as detailed in Section 4.4. The integration of Newton's equations of motion is then performed using a fifth order Gear's predictor-corrector algorithm [61] for translational and rotational degrees of freedom. This integration scheme is discussed in Section 4.1. The normal force is calculated by the nonlinear Hertzian model with the dissipation term also nonlinear. For the tangential force a linear-dashpot model is employed. These force models are discussed in detail in Section 4.2. We also discuss, subsequently, in Section 4.3, the choice of values for parameters and the interactions between the grains and the walls. Finally, in Section 4.4 , we discuss the initial configuration and the reinsertion procedure.

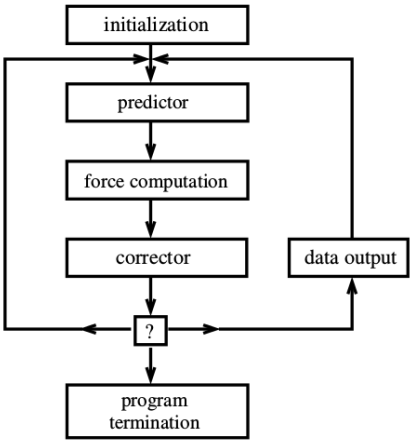

Figure 6: The algorithm of the simulation is presented in a flowchart. Figure reproduced from [61].

4.1 Integration of Newton's Equations of Motion

We perform the integration of the Newton's Equations of Motion via a fifth order Gear's predictor-corrector algorithm. For that, we need to compute the evolution of each coordinate derivatives up to fourth order. The rotational coordinates are somewhat more complicated and will be discussed separately. This algorithm presents numerical errors growing as $(\Delta t)^5$ which is lower than the precision of a real number in the computer implementation we used. The efficiency dependence of the code on the integration method and order is not a key factor, as the procedures for contact check and force evaluation are more computationally expensive. Gear's scheme is more convenient for the integration of the differential equations than other methods when the forces and torques depend on the translational and rotational velocities [75].

Predictor

First, we compute the prediction of the system state. This computation consists of extrapolating the values of coordinates and their derivatives at time $t+\Delta t$ from the Taylor expansion of their current values, which reads

$$\begin{aligned}
\vec{r}_i^{\,pr}(t+\Delta t) &= \vec{r}_i(t) + \Delta t\ \dot{\vec{r}}_i(t) + \tfrac{1}{2}\Delta t^2\ \ddot{\vec{r}}_i(t) + \tfrac{1}{6}\Delta t^3\ \vec{r}_i^{\,(3)}(t) + \tfrac{1}{24}\Delta t^4\ \vec{r}_i^{\,(4)}(t) \\
\dot{\vec{r}}_i^{\,pr}(t+\Delta t) &= \dot{\vec{r}}_i(t) + \Delta t\ \ddot{\vec{r}}_i(t) + \tfrac{1}{2}\Delta t^2\ \vec{r}_i^{\,(3)}(t) + \tfrac{1}{6}\Delta t^3\ \vec{r}_i^{\,(4)}(t) \\
\ddot{\vec{r}}_i^{\,pr}(t+\Delta t) &= \ddot{\vec{r}}_i(t) + \Delta t\ \vec{r}_i^{\,(3)}(t) + \tfrac{1}{2}\Delta t^2\ \vec{r}_i^{\,(4)}(t) \\
\vec{r}_i^{\,(3)\ pr}(t+\Delta t) &= \vec{r}_i^{\,(3)}(t) + \Delta t\ \vec{r}_i^{\,(4)}(t) \\
\vec{r}_i^{\,(4)\ pr}(t+\Delta t) &= \vec{r}_i^{\,(4)}(t)
\end{aligned} \quad , \tag{4.1}$$

where $\vec{r}_i(t)$ is the position vector for particle i, $\dot{\vec{r}}_i(t)$ is its first time derivative, the velocity, and $\ddot{\vec{r}}_i(t)$ is the acceleration or second time derivative. Further time derivatives are $\vec{r}_i^{\,(3)}$ and $\vec{r}_i^{\,(4)}$ for derivatives of third and fourth order, respectively, as for the fifth order Gear's scheme, the derivatives of spatial coordinates are retained until fourth order. The superscript pr indicates the predicted coordinates.

Corrector

The corrector step is carried out after the evaluation of the forces based on the predicted system configuration. These forces are used to provide the values for the acceleration

coordinates, $\ddot{\vec{r}}_i^{\,c}(t+\Delta t)$, and from that the correction of the position vector and remaining derivatives are obtained as

$$\begin{pmatrix} \vec{r}_i^{\,c}(t+\Delta t) \\ \dot{\vec{r}}_i^{\,c}(t+\Delta t) \\ \ddot{\vec{r}}_i^{\,c}(t+\Delta t) \\ \vdots \end{pmatrix} = \begin{pmatrix} \vec{r}_i^{\,pr}(t+\Delta t) \\ \dot{\vec{r}}_i^{\,pr}(t+\Delta t) \\ \ddot{\vec{r}}_i^{\,pr}(t+\Delta t) \\ \vdots \end{pmatrix} + \begin{pmatrix} c_0 \\ c_1 \frac{1}{(\Delta t)} \\ c_2 \frac{2}{(\Delta t)^2} \\ \vdots \end{pmatrix} \frac{(\Delta t)^2}{2} \Delta\ddot{\vec{r}}\,. \tag{4.2}$$

As before, the superscript pr indicates the predicted coordinates, whereas c represents the corrected ones. Also, $\Delta\ddot{\vec{r}} = \ddot{\vec{r}}_i^{\,c} - \ddot{\vec{r}}_i^{\,pr}$ and the coefficients c_i for $i = 0, 1, 2, 3, 4$ are dependent on the order of the method and whether the forces depend on the velocities or not. And, as deduced by Gear himself, for the fifth order Gear's scheme with velocity dependent forces they are [61, 75, 76, 77]

$$c_0 = \frac{19}{90}; \quad c_1 = \frac{3}{4}; \quad c_2 = 1; \quad c_3 = \frac{1}{2}; \quad c_4 = \frac{1}{12}.$$

4.1.1 Rotational Coordinates: Quaternions

In order to describe the position of a particle in three dimensions, beyond the three spatial coordinates, one needs three angles to map the orientation of the particle in motion. These angles relate two coordinate systems: the *body system* and the *co-moving system*. The co-moving system axes are parallel to those of the laboratory system which is used to track the translational motion of the particles, however,they are centered at the center of mass of the particle. In the co-moving system the particle motion is purely rotational. The center of mass is also the origin of the body system, however,its axes follow the rotational motion of the particle and it is useful to choose them to coincide with the principal axes of rotation of the particle. In fact, when the body system is defined in this way the moment of inertia tensor is constant and diagonal, independently of the shape of the particle, and therefore the computations required in the simulation are greatly simplified[1]. Another system has to be defined, the *frozen system*. This system coincides with the body system at a fixed time t. This guarantees that we are working on an inertial system as long as we take the frozen system relative to the time instant that we are performing each calculation.

[1]We present here the procedures for the simulation of general shaped particles, as it was implemented in our code. Nevertheless, the results presented in this Thesis are restricted to spherical grains, for which most of the discussion in this session regarding the inertia moment and other aspects of the rotational movement are much simpler.

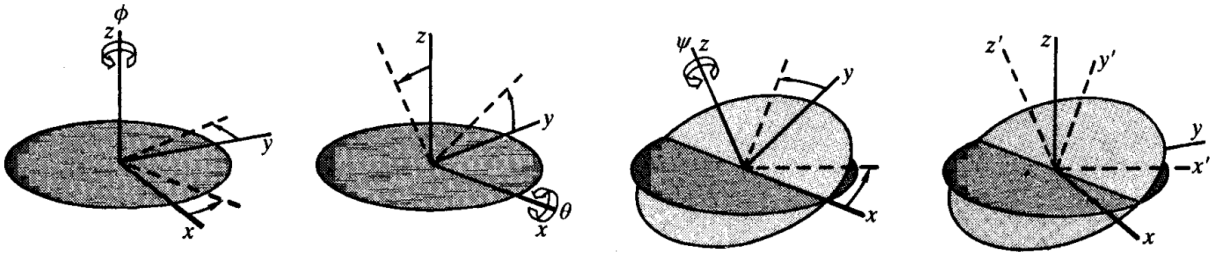

Figure 7: Euler angles are defined. Figure adapted from [75].

The transformation between two systems with coinciding origins can be represented by the *Euler angles*. They are presented in Figure 7 as each accounts for one of the three rotations that are performed for the transformation. Those angles are the parameters of the rotation matrix that, applied to a vector of the co-moving system, will provide the corresponding vector in the frozen system. The rotation matrix, A, can be written in this case as

$$A = \begin{pmatrix} \cos\phi\cos\psi - \sin\phi\cos\theta\sin\psi & \sin\phi\cos\psi + \cos\phi\cos\theta\sin\psi & \sin\theta\sin\psi \\ -\cos\phi\sin\psi - \sin\phi\cos\theta\cos\psi & -\sin\phi\sin\psi + \cos\phi\cos\theta\cos\psi & \sin\theta\cos\psi \\ \sin\phi\sin\theta & -\cos\phi\sin\theta & \cos\theta \end{pmatrix} . \tag{4.3}$$

If the particle is rotating, the Euler angles describing the transformation from the co-moving system to the frozen system are also changing and their derivatives are related to the angular velocities of the particle in the co-moving system, w_i^{cm} $(i = x, y, z)$, as

$$\begin{aligned} \dot{\phi} &= - w_x^{cm} \frac{\sin\phi\cos\theta}{\sin\theta} + w_y^{cm} \frac{\cos\phi\cos\theta}{\sin\theta} + w_z^{cm} \\ \dot{\theta} &= w_x^{cm} \cos\phi + w_y^{cm} \sin\phi \\ \dot{\psi} &= w_x^{cm} \frac{\sin\phi}{\sin\theta} - w_y^{cm} \frac{\cos\phi}{\sin\theta} . \end{aligned} \tag{4.4}$$

This matrix involves the reciprocal of trigonometrical functions of the angles and is, therefore, prone to numerical instabilities when the trigonometrical function tends to zero. A solution for this issue is the representation of the angles by four-dimensional vectors known as quaternions, (q_0, q_1, q_2, q_3) that can map the Euler angles. The quaternions lie on a four-dimensional sphere

$$q_0^2 + q_1^2 + q_2^2 + q_3^2 = 1 , \tag{4.5}$$

they can be obtained from the Euler angles, if defined as in Figure 7, as

$$\begin{aligned} q_o &= \cos\tfrac{1}{2}\theta \ \cos\tfrac{1}{2}(\phi+\psi) \\ q_1 &= \sin\tfrac{1}{2}\theta \ \cos\tfrac{1}{2}(\phi-\psi) \\ q_2 &= \sin\tfrac{1}{2}\theta \ \sin\tfrac{1}{2}(\phi-\psi) \\ q_3 &= \cos\tfrac{1}{2}\theta \ \sin\tfrac{1}{2}(\phi+\psi) \end{aligned} \tag{4.6}$$

and the rotation matrix becomes

$$A = \begin{pmatrix} q_0^2+q_1^2-q_2^2-q_3^2 & 2(q_1q_2+q_0q_3) & 2(q_1q_3-q_0q_2) \\ 2(q_1q_2-q_0q_3) & q_0^2-q_1^2+q_2^2-q_3^2 & 2(q_2q_3+q_0q_1) \\ 2(q_1q_3+q_0q_2) & 2(q_2q_3-q_0q_1) & q_0^2-q_1^2-q_2^2+q_3^2 \end{pmatrix}. \tag{4.7}$$

Therefore, a vector in the frozen system, $\vec{u}^{\,f}$, is obtained from the original in the co-moving system, $\vec{u}^{\,cm}$, as $\vec{u}^f = A\vec{u}^{\,cm}$.

The quaternion first derivative can obtained from the quaternion itself and the angular velocity vector [75], as

$$\begin{pmatrix} \dot{q}_o \\ \dot{q}_1 \\ \dot{q}_2 \\ \dot{q}_3 \end{pmatrix} = \frac{1}{2} \begin{pmatrix} q_0 & -q_1 & -q_2 & -q_3 \\ q_1 & q_0 & -q_3 & q_2 \\ q_2 & q_3 & q_0 & -q_1 \\ q_3 & -q_2 & q_1 & -q_0 \end{pmatrix} \begin{pmatrix} 0 \\ w_x^f \\ w_y^f \\ w_z^f \end{pmatrix}, \tag{4.8}$$

where w_x^f is the x-axis component of the angular velocity in the frozen system of coordinates. This equation is obtained by performing the time derivative of the relations between the quaternion components and the Euler angles, equation 4.6, and using the relations between the Euler angles and the angular velocities, equation 4.4. The transformation of the angular velocities from the co-moving system and the frozen system is also necessary, which is accomplished via the matrix A from equation 4.7.

We will also need to do the opposite, that is, to obtain the angular velocity from the quaternion first derivative. Such a transformation is given by

$$\begin{pmatrix} w_x^f \\ w_y^f \\ w_z^f \end{pmatrix} = 2 \begin{pmatrix} -q_1 & q_0 & q_3 & -q_2 \\ -q_2 & -q_3 & q_0 & q_1 \\ -q_3 & q_2 & -q_1 & q_0 \end{pmatrix} \begin{pmatrix} \dot{q}_o \\ \dot{q}_1 \\ \dot{q}_2 \\ \dot{q}_3 \end{pmatrix}. \tag{4.9}$$

Having the quaternions and their derivatives we can perform a Gear's predictor step in complete analogy to what is done for the spatial coordinates. The procedure is applied

to all four dimensions of the quaternions. We need to compute the contribution of the torques only before the corrector step of the integration to obtain the angular acceleration vectors. This is done via the rotational equation of motion

$$\overleftrightarrow{I}\dot{\vec{w}}^f = \vec{T}^f - \vec{w}^f \times \overleftrightarrow{I}\vec{w}^f \tag{4.10}$$

or, more clearly,

$$\dot{w}_i^f = \frac{1}{(I)_{ii}}\left[\vec{T}_i^f + (I_{jj} - I_{kk})w_j^f w_k^f\right] \ , \tag{4.11}$$

where i, j and k follow the usual cyclic permutations. $\vec{T}^f$ is the torque in the frozen system of coordinates acting on the particle, which is obtained from the torque acting in the particle due to interactions with other particles and with the walls, however,it is necessary to transform it from the co-moving system to the frozen system by the application of the transformation matrix in equation 4.7. To transform the angular acceleration vector, $\dot{\vec{w}}^f$, to the quaternion representation, we differentiate equation 4.8 to obtain

$$\begin{pmatrix} \ddot{q}_o \\ \ddot{q}_1 \\ \ddot{q}_2 \\ \ddot{q}_3 \end{pmatrix} = \frac{1}{2}\begin{pmatrix} q_0 & -q_1 & -q_2 & -q_3 \\ q_1 & q_0 & -q_3 & q_2 \\ q_2 & q_3 & q_0 & -q_1 \\ q_3 & -q_2 & q_1 & q_0 \end{pmatrix} \cdot \begin{pmatrix} -2\sum_{m=0}^{3}\dot{q}_m^2 \\ \dot{w}_x^f \\ \dot{w}_y^f \\ \dot{w}_z^f \end{pmatrix} . \tag{4.12}$$

Therefore the calculation of the angular acceleration is only an intermediate step in order to obtain the quaternion second derivative, which is necessary for the corrector step of the integration playing the same role as the acceleration in the spatial coordinates integration.

At the end of each time step the quaternions should be renormalized as, due to numerical errors, their norm may differ from the unit after the calculations. The unit norm of the quaternions, as expressed in Equation 4.5, is part of their definition and the validity of every equation involving the quaternions depends on such normalization.

The procedure can be summarized as follows,

- the predictor step is performed on the four components of the quaternion and its derivatives in complete analogy to the spatial coordinates;
- the forces and torques are calculated based on the predicted spatial coordinates and angular velocities in the laboratory (co-moving) coordinate system which are obtained from the predicted quaternion first derivative through equation 4.9;
- the quaternion second derivative is obtained from the torques through equations 4.11 and 4.12 combined;

- the corrector step is performed on the four components of the quaternions exactly as for the spatial coordinates;
- after that, the quaternions are renormalized to guarantee Equation 4.5 to hold.

4.2 Forces

The grains, in our simulations, are subject to forces due to the action of gravity and, possibly, to the contact with other grains. The most simple of those forces, weight, $\vec{W}$, acts homogeneously with acceleration of gravity, g, constant in the negative z-direction, thus, simply,

$$\vec{W} = -mg\hat{k},$$

where m is the mass of the grain. The model for the forces acting on the interaction between pairs of grains can be separated into normal and tangential components. We present each of such components in the following subsections.

4.2.1 Normal Force

A solid material in the elastic regime presents a restoring force when deformed. For a pair of spherical homogeneous particles of the same material, the repulsion force due to deformation when they are pressed together was deduced from the theory of elasticity by Hertz [78, 79, 80]. It was shown that the force is proportional to the area of the disk of deformation, which is in turn a function of the overlap length. That is the length of the deformation measured in the direction connecting the centers of the two particles, see Figure 8a. In simulations, the particles are allowed to interpenetrate, however, in reality, the particles are deformed, as it is shown schematically in Figure 8b.

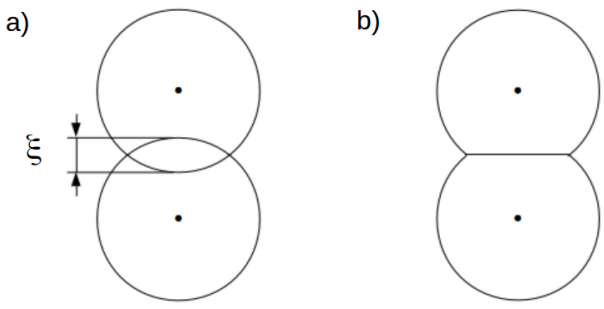

Figure 8: Schematic figure showing interaction of spherical particles. a) particles in simulation are allowed to interpenetrate and overlap length, ξ, is shown; b) in corresponding real situation the particles are deformed.

For a spherical grain particle i, with radius R_i and at position $\vec{r}_i$, in contact with particle j the overlap length is $\xi = [(R_i + R_j) - |\vec{r}_j - \vec{r}_i|]$, where $\xi < 0$ means there is no contact. The Hertzian Law for the normal force f_n is, then, written as

$$f_n = E\, R_{\text{eff}}^{1/2}\, \xi^{3/2}, \tag{4.13}$$

where $R_{\text{eff}} = (R_i^{-1} + R_j^{-1})^{-1}$ is the effective radius and $E = (2/3)[Y/(1-\nu^2)]$ is the elastic coefficient, in which Y is the Young modulus and ν is the Poisson ratio of the material [78, 79, 80].

Equation 4.13, however, does not account for the dissipation that occurs in real collisions between spherical particles. There are many models for the dissipative contribution of the normal force in the literature, each presenting different accuracies when compared to experiments [61, 81]. Among those, we have chosen the nonlinear model proposed by Kuwabara and Kono [82] and later independently deduced by Brilliantov *et al.* [83]. It has been widely applied in the literature due its good agreement with experiments on the dependence of the coefficient of restitution and of the collision time with the impact velocity for a pair of spheres in the viscoelastic regime for many materials [84, 81]. It can be written as

$$F_n = E\, R_{\text{eff}}^{1/2} \left(\xi^{3/2} + A\xi^{1/2}\dot{\xi}\right), \tag{4.14}$$

where $\dot{\xi}$ is the normal relative velocity and A is a normal damping constant. We will postpone the discussion on the nature and values of the parameters, including the damping constant A, to the following section.

We also impose positive values for f_n, so that attractive forces are avoided, as those would lead to unphysical behavior for dry granular material. Therefore, the normal force vector is

$$\vec{F}_n = \max(0, f_n)\, \hat{e}_n, \tag{4.15}$$

where $\hat{e}_n = (\vec{r}_j - \vec{r}_i) \,/\, |\vec{r}_j - \vec{r}_i|$ is the normal unit vector.

4.2.2 Tangential Force

Frictional forces are present in most collisions between real particles due to their surface texture. The only exception is if no relative tangential velocity vector acts at the point of contact between the spheres during the whole collision time, as happens for a head-on collision of non-rotating particles. That is a very unlikely situation for a dense packing of flowing granular material. Therefore, the tangential forces generated by friction

are an important feature of the system of interest and should be carefully accounted for in the simulation. The tangential force between a pair of particles is, as discussed, frictional, and follows the Coulomb criterion that separates the static and the dynamic regimes. In the dynamic regime the particles slide on each other while a frictional force acts on each particle and is proportional to the normal force at the point of contact. The dynamic friction coefficient, μ_d, is the proportionality factor so that the dynamic tangential force is

$$F_d = \mu_d F_n. \tag{4.16}$$

Coulomb's law of friction states that, in the static regime, the frictional tangential force exactly counterbalances the applied tangential force preventing the particles from slipping over each other. However, computationally this procedure is unfeasible as such applied tangential force is unknown in most cases. Many approaches exist to circumvent this issue, usually by, paradoxically, allowing a small relative tangential motion in the static regime.

The tangential force in the static regime is modeled in our simulation as a linear viscoelastic dashpot in the spirit of Cundall and Strack's seminal paper [85] and it is implemented following the description by Luding [86]. The displacement for the elastic term of the force is obtained by considering a spring having one end attached to the point on the surface of the particle of interest that was first in contact with the incident particle and the other end of the spring being placed at the current point of contact, those are, respectively, point A and point B in Figure 9. The dissipative term is a simple viscous term linearly dependent on the tangential relative velocity, $\vec{v}_t = \vec{v}_{ij} - \hat{e}_n(\hat{e}_n \cdot \vec{v}_{ij})$. Therefore the force in the static regime is

$$\vec{F}_s = -k_t\vec{\zeta} - \gamma_t\vec{v}_t\,, \tag{4.17}$$

where $\vec{\zeta}$ is the spring tangential displacement, k_t is the spring stiffness, γ_t is the tangential damping constant and, as mentioned, $\vec{v}_t$ is the tangential relative velocity. Only the tangential displacements are considered, so that $\vec{\zeta}$ and $\vec{v}_t$ are parallel to each other [86].

The Coulomb criterion dictates that if F_s is larger than the static friction limit, that is $F_s > \mu_s F_n$, where μ_s is the coefficient of static friction, then the particles are in the dynamic regime. Therefore, the tangential force is

$$\vec{F}_t = \hat{e}_t \cdot \begin{cases} F_s & \text{if } F_s \leq \mu_s F_n \text{ (static regime)} \\ F_d & \text{if } F_s > \mu_s F_n \text{ (dynamic regime).} \end{cases} \tag{4.18}$$

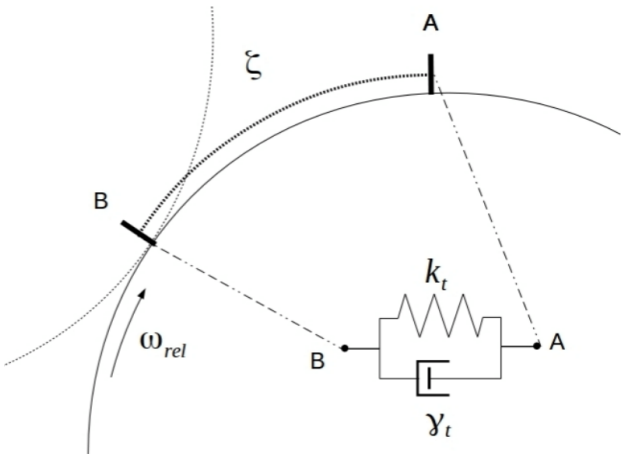

Figure 9: Schematic figure showing tangential force model. Spring displacement, ζ, is measured as the distance between the point of first contact, A, and point of current contact, B. Force follows linear dashpot model.

4.2.3 Wall-Grain Force

In our simulations we use conical hoppers or conical bottom silos. The walls are simulated by the force law given by equations 4.15 and 4.18. The overlap length ξ is calculated using a similar approach to the pairwise collision, but considering the portion of the grain that penetrates the wall surface, as seen in Figure 10a. Additionally, R_{eff} is considered to be equal to the radius of the grain. This is consistent with the previous definition in the limit of the wall radius going to infinite, that is, a radius much larger than the radius of the particle. This model for the normal force is consistent with that obtained from Theory of Elasticity for the stresses between a sphere and a plane wall [80], and as such it is an approximation of the problem at hand.

We simulate the orifice edge thickness in order to avoid spurious behavior of out-pouring particles, which was commonly observed in preliminary simulations of elongated grains. It is done by considering a virtual particle on the border of the hopper, its position being such that its center lies on the plane defined by the z-axis and the center of the colliding grain, see Figure 10b. The virtual particle radius is set $R_G = \frac{1}{2}R$, hence the wall thickness is equal to 5 mm, a reasonable choice for the walls of a metal hopper.

The material parameters are set to be equal to those of collisions between grains.

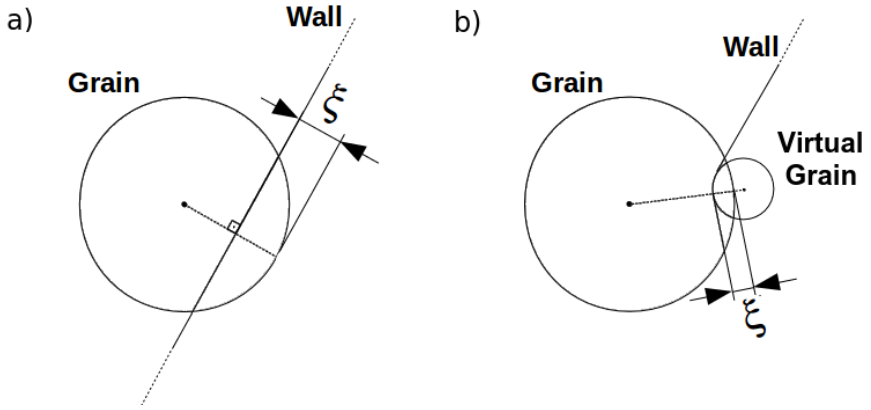

Figure 10: The overlap length is shown for the wall-grain collisions. a) A grain is in contact with the bulk of the conical wall; b) a grain is in contact with the border of the hopper, which is simulated by a virtual grain.

4.3 Parameters

We shall discuss the choice for material parameters throughout this section, nonetheless they are summarized here as: $E = 10^8$ Pa, corresponding to $Y \simeq 10^8$ Pa and $\nu \simeq 10^{-1}$, $\mu_s = 0.8$, $\mu_d = 0.6$, $k_t = 100$ N/m, $\gamma_t = 0.1$ Kg/s, $A = 0.01$ s. In order to avoid crystallization, which occurs in dense packings of identical spheres, the radii of the spheres are randomly chosen from a uniform distribution with tolerance of 5% around $R = 5$ mm. The density is 8×10^3 kg/m^3, therefore grain weights range from 3.6 g up to 4.8g. Additionally to contact forces, gravity acts on each particle and the acceleration of gravity in the simulations is set to $g = 10$ m/s^2 in the direction of $-\hat{z}$. The time step was chosen as $\Delta t = 10^{-6}s$ in order to guarantee it was, typically, at least 20 times smaller than the collision time. For each system, 20000 grains were simulated.

The value for the parameter E is intrinsically related to the Young modulus, Y, and the Poisson ratio, ν, by the equation

$$E = (2/3)[Y/(1-\nu^2)].$$

Nevertheless, the Poisson ratio plays a very small role, as its experimental values typically range from 0.2 up to 0.5 [87], and then the factor $2/3(1-\nu^2)$ ranges from 0.69 to 0.89, not affecting the order of magnitude of E. In fact, the value of E is dominated by the Young modulus. For materials used in the experiments or in simulations, these values range over many orders of magnitude. We choose the value of $E = 10^8$ Pa which represents a Young modulus of the same order of magnitude, that is, $Y \simeq 10^8$ Pa, which is a realistic value and contributes to enabling larger time steps on the simulation.

The dissipative term in the normal force carries the damping parameter A, which is related to properties of the material that are not usually experimentally known and not easily measurable, namely the viscosity of the grain material [83]. Because of that, this parameter value is chosen so that the simulation results agree to some experimental data. We have chosen $A = 0.01s$ following the book by Pöschel [61]. As the force model is non linear, the coefficient of restitution depends on the initial relative velocity of the pair of colliding grains.

The static and dynamic friction coefficients, $\mu_s = 0.8$ and $\mu_d = 0.6$, were chosen among the values commonly found in materials used on experiments, such as steel [88]. The other parameters that contribute to the tangential force are those employed on the linear-dashpot force. This model, as discussed, represents the static tangential force by a linear elastic force as that of a spring and a damping term dependent on the relative tangential velocity. The spring constant value is chosen in order to guarantee that the spring displacement is small enough compared to the grain radius when the static regime limit is reached. This can be done by comparing the elastic term of this force to the Coulomb criteria: $\mu_s F_n < \zeta k_t$, which means that the collision will enter the dynamic friction regime for larger spring displacements. If we expect that $\zeta << R$, say $\zeta \sim R/20$, it means $k_t \sim \frac{\mu_s \max(F_n)}{R/20}$ and, considering $\max(F_n) \approx 20$N, it yields $k_t \sim 10^5 N/m$. Another consideration to be taken on the value of k_t is that raised by the paper by Schaeffer et al. [84] [2] . The collision time for the tangential force and for the normal force must be synchronized, that is $t_s/t_n \sim 1$. From [84], we know that $t_n = 3.21 \left(\frac{m_{\text{eff}}}{k_n}\right)^{2/5} v_n^{-1/5}$ and $k_t = \frac{2}{7} m_{\text{eff}} \left(\frac{\pi}{t_s}\right)^2$ and, given that, we want that $t_s \sim t_n$, we can show that $k_t \sim 6 \times 10^4 N/m$, which is well represented by our value since the nonlinearity of the normal force already makes the argument not so rigorous.

Finally, regarding the values for the tangential viscosity, $\gamma_t = 0.1$Kg/s, it should be noted that the damping term must be much smaller than the elastic term for typical situations. That is, $\gamma_t v_t << \zeta k_t$, yielding, for the typical cases, $\gamma_t << 10$Kg/s which validates our choice for the value of this parameter.

[2] This issue was brought to our attention during the revision process of our paper [89] by one of the referees, Prof Luis Pugnaloni.

4.4 Initialization and Reinsertion

The system is initialized by one of two processes. The simplest procedure is done by releasing the grains from a regular cubic lattice configuration inside the hopper with the grain centers separated typically by $3R$ or $4R$ with random velocities homogeneously distributed within a small range around zero while the hopper orifice is kept closed. The orifice is only opened after a time of typically 0.5 s (5×10^5 time steps), which ensures that the velocity of the grains is much smaller than that they attain during the discharge. After that, the discharge procedure begins.

This procedure demands a long computation time for the settling of the system, therefore a more efficient solution was later developed using a third party package. For this second procedure we take advantage of Packmol®, a package designed to create initial configurations for molecular dynamics simulations [90]. We use Packmol® to produce tight packings of grains in the hoppers, which diminishes the time needed for the settling of the grains, compared to that of the former procedure, where the grains were much looser.

In order to maintain a stationary flow, grains that are more than one diameter below the outlet are reinserted at randomly chosen positions at the top surface of the material in the hopper. This procedure is carried out at regular intervals of 0.1 s (10^5 time steps). Thus, the number of particles inside the hopper is kept approximately constant throughout the discharging process.

5 *Velocity Profiles and Flow Regimes*

We investigate the flow regime during discharge of spherical grains through a conical hopper. As discussed in the Introduction, that is, Chapter 1, granular flow through apertures has been historically classified either as in mass flow or funnel flow regimes. Throughout this chapter, we discuss the index that is commonly applied to classify such regimes, the Mass Flow Index, and we propose a generalization, where the spatial coordinate is kept. This generalization avoids sensibility on the protocol chosen to obtain the index and we believe that may lead to better classification of the flow regimes.

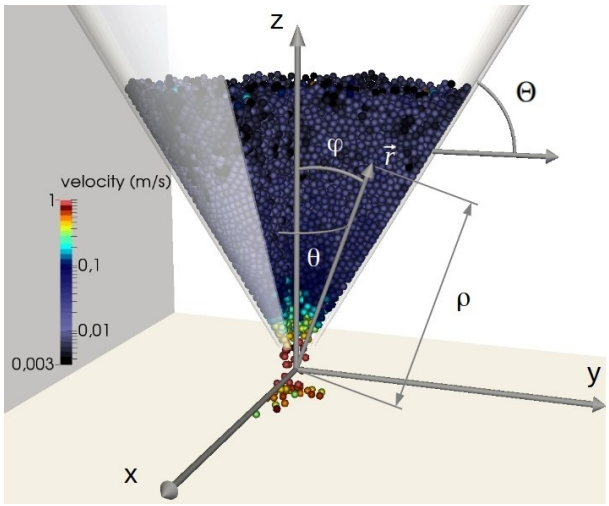

Figure 11: Snapshot of the system shows the hopper and flowing grains. Cartesian and spherical coordinates are shown, respectively, as (x, y, z) and (ρ, θ, φ). Note that, as the origin of the coordinate systems coincides with the hopper vertex, there is a distance $\rho_0 = D/2 \cos\Theta$ from the origin to the edge of the hopper along directions of ρ parallel to the walls

A snapshot of the system configuration can be seen in Figure 11. The Cartesian and spherical coordinate systems are shown, which are represented, respectively, as (x, y, z) and (ρ, θ, φ). The direction of the position vector projected onto the horizontal plane defines the r axis, so that the $r - z$ plane includes the current point of interest and the z

axis. For both Cartesian and spherical systems, the origin is chosen to coincide with the cone vertex. Also, the hopper angle with the horizontal plane, Θ, is defined. The orifice diameter, not shown in the figure, is represented by the letter D and presented in units of R, the average grain radius.

5.1 Velocity Fields

In order to visualize the steady-state flow, we create a velocity field. That is obtained by constructing a regular square cell grid on a longitudinal plane crossing the z axis, where the average of the modulus of the velocity is taken over grains which center is inside that cell or the neighboring cells, seen in Figure 12a. Note that, due to the azimuthal symmetry, each cell is a ring of square section of sides equals to 0.002 m, as shown in Figure 12b. However as the averages are considered over an extended cell that includes the neighboring cells, the averaging region presents square cross-section of side 0.006 m. This procedure allows a finer picture, while it avoids an increase of statistical errors. The ring radius depends on the cell position on the $r - z$ plane and therefore the volumes are different. Additionally, the velocity is averaged over time from snapshots taken regularly during the whole simulation. The snapshots are taken every 0.005 s to avoid redundancy and the duration of each simulation is typically between 5 s and 10 s.

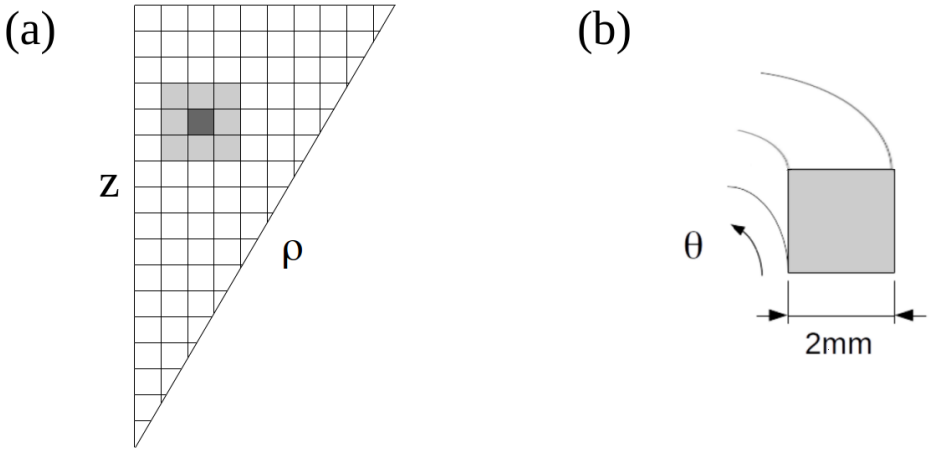

Figure 12: Schematic figure showing averaging region for velocity fields. a) grid of cells, in dark gray the cell for which the averaged value will be associated and in light gray the neighboring cells that contribute to the average. b) each cell is the cross-section of a square torus due to the azimuthal coordinate, θ. Also the size of the sides of each cell is shown to be equal to 2 mm.

The velocity fields are shown in Figure 13 for a few choices of orifice widths. Note that, by increasing the orifice size, the overall velocity increases. The iso-velocity curves, i.e.

the borderline between two different color shades, are always crossing the entire horizontal extension of the hopper for orifice size $D = 8R$, while for $D = 16R$ and $D = 24R$ there are closed curves close to the wall. Also, the general shape of these curves changes with the orifice size, being more horizontal for smaller orifice sizes and increasingly inclined for larger ones. This means that for the same distance from the vertex of the hopper the average velocity of the grains is larger at the center of the hopper than close to its walls.

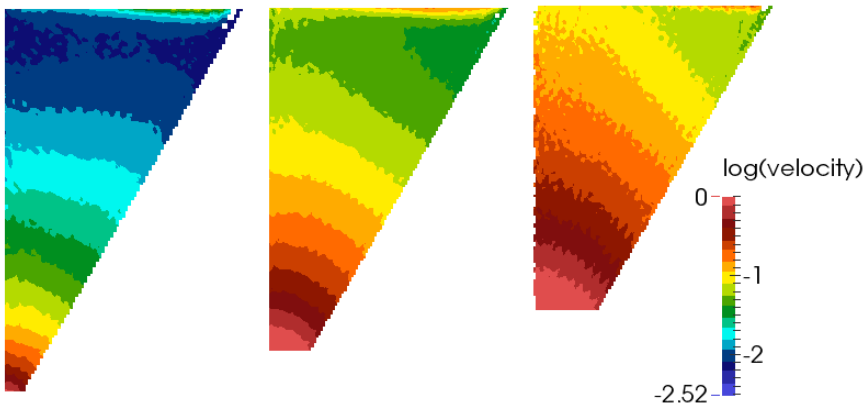

Figure 13: Velocity field is presented in color scale for $\Theta = 60°$ and $D = 8R, 16R$ and $24R$, from left to right. Color scale is the modulus of the averaged velocity in units of log(m/s). Each cell is the rectangular section of a ring with sides equals to 0.002 m, however, the average of the velocity is taken over grains belonging this and the neighboring cells. The top of the hopper was cropped to avoid showing the free surface, where reinsertion dynamics dominates.

The velocity field analysis may be useful to differentiate extreme states such as a fully developed funnel flow and a very typical mass flow. However, it is not appropriate to distinguish more subtle flow differences, as the analysis is based on the visual aspect of the field and qualitative in nature.

5.2 Velocity Radial Profiles and the Local Mass Flow Index

In order to characterize the flow more quantitatively, we contrast the two most different regions of the hopper, that is, we compute the velocity profile along ρ, the radial distance from the hopper cone vertex (Figure 11), close to the wall of the hopper, $v_{\mathrm{w}}(\rho)$, and along its central line, $v_{\mathrm{c}}(\rho)$. These velocities are computed in a similar procedure to that of the velocity field. However, the sides of the square cells for the wall velocity are taken parallel and perpendicular to the walls of the hopper. Furthermore, we generalize the concept of Mass Flow Index, as discussed in the Introduction of this Thesis, to a Local

Mass Flow Index profile, $I_{\mathrm{LMF}}(\rho)$. It can be obtained directly from the velocity profiles as

$$I_{\mathrm{LMF}}(\rho) = \frac{v_{\mathrm{w}}(\rho)}{v_{\mathrm{c}}(\rho)}.$$

The only example of a similar localized index we have seen in literature was in a paper by González-Montellano *et al.* [26]. Nevertheless, they did not consider it as a profile and mainly used it to compare the behavior of the flow in the hopper section with that in the bin section of a silo. As discussed in the Introduction, they have calculated the index for a few positions scattered along the silo as a secondary assessment of the shape of the horizontal velocity profile, which was their main subject.

We apply this analysis to data from simulations of discharges in hoppers of different orifice sizes, see Figure 14. The larger fluctuations seen in the center velocity profiles compared to the wall velocity are due to the smaller averaging volume as, due to the azimuthal symmetry, the volumes are larger the farther from the z axis. We have chosen this procedure, despite the different averaging volumes as, due to the symmetry, we expect no change in the behavior of the wall velocity profile if the average was performed over a region of smaller volume. A restriction on the use of data that is at our disposal would unnecessarily increase statistical noise. In panel 14a, a power law decay is observed for the velocity profiles along ρ. As discussed before, this behavior is not surprising, however, discrepancies between v_{w} and v_{c} are visible. We believe that these discrepancies carry information about the flow regime and should not be disregarded. For small orifice sizes, namely $D = 6R$ and $D = 8R$, the slope of the velocity along the center of the hopper appears to be larger than that along the walls, until they collapse into approximately the same curve further up in the hopper. On the other hand, for large orifice sizes, $D = 16R$ and $D = 24R$, there is a large gap between v_{c} and v_{w} all along ρ, and the slopes are very similar. Therefore, the gap is approximately constant even for large ρ.

One could have analyzed this also through the I_{LMF} in Figure 14b. The simulations with small opening diameters show I_{LMF} curves tends to increase with ρ, starting from $I_{\mathrm{LMF}} \simeq 0.8$ until they reach values close to unity, meaning the wall and center velocities are approaching identical values at higher positions. On the other hand, the curves for large opening widths present smaller values — $I_{\mathrm{LMF}} \simeq 0.65$ for $D = 24R$ —a consequence of the gap between v_{c} and v_{w}.

As discussed, the commonly used Mass Flow Index may depend on the position and size of averaging windows. The reason for this is made clear in Figure 14a where the power law decaying velocity profile is confirmed. Moreover, the classification of the funnel flow

regime as that in which $I_{\mathrm{MF}} < 0.3$ is, then, questionable. Contrastingly, the Local Mass Flow Index, proposed here, is capable of distinguishing the typical mass flow behavior, such as the cases where $D = 6R$, $8R$ and $12R$, from another regime where there are large differences between the center and wall velocities, even though stagnation zones are absent, cases $D = 16R$ and $24R$. This seems to be a precursor of the funnel flow regime where the wall velocity is much smaller than the center velocity all along the hopper.

By the usual definition of the Mass Flow Index, we estimate values close to $I_{MF} \simeq 0.75$ for the five situations described in Figure 14. However, we note differences of over 30% between the I_{LMF} of each case. This occurs because the average of a quantity which varies with a power law, such as the grain velocity, can lead to incorrect data interpretation.

Additionally, we present the analogous velocity profiles for hoppers of different opening angles, Figure 15a. The same general behavior is observed, that is, a power law for both velocities. Differences between v_{c} and v_{w} are larger close to the outlet and decrease with increasing ρ. It is interesting to note that the I_{LMF} curves for all angle Θ, in Figure 15b, are identical within the fluctuation range. This is a very interesting effect that we intend to investigate further for other opening angles, but which will cost a considerable computational effort. Comparing the I_{LMF} with the I_{MF} values, we can observe again that the latter is considerably less sensitive to velocity fluctuations than the former. Again, we believe that this discrepancy is due to the averaging of a power law quantity, which is not a well defined quantity subject to large fluctuations.

According to the literature [22, 31], the velocity radial profiles should decay as a power law with exponent equals to 2, as calculated for an incompressible fluid in the introduction of this chapter. For all the cases, we obtained exponents around that value, the smallest value being 1.868(3) for $D = 12R$ and $\Theta = 45°$ and the largest value being 2.176(5) for $D = 24R$ and $\Theta = 60°$, both for the wall velocity profile. However, we observe in Figures 14a and 15a that for the center velocity the slope of the profile varies along ρ. This is easily observed, for instance, for $D = 12R$ and $\Theta = 45°$ (lower curves in Figure 15a) where the center and wall velocity profiles are very close and approximately parallel for large ρ, but they separate close to the orifice.

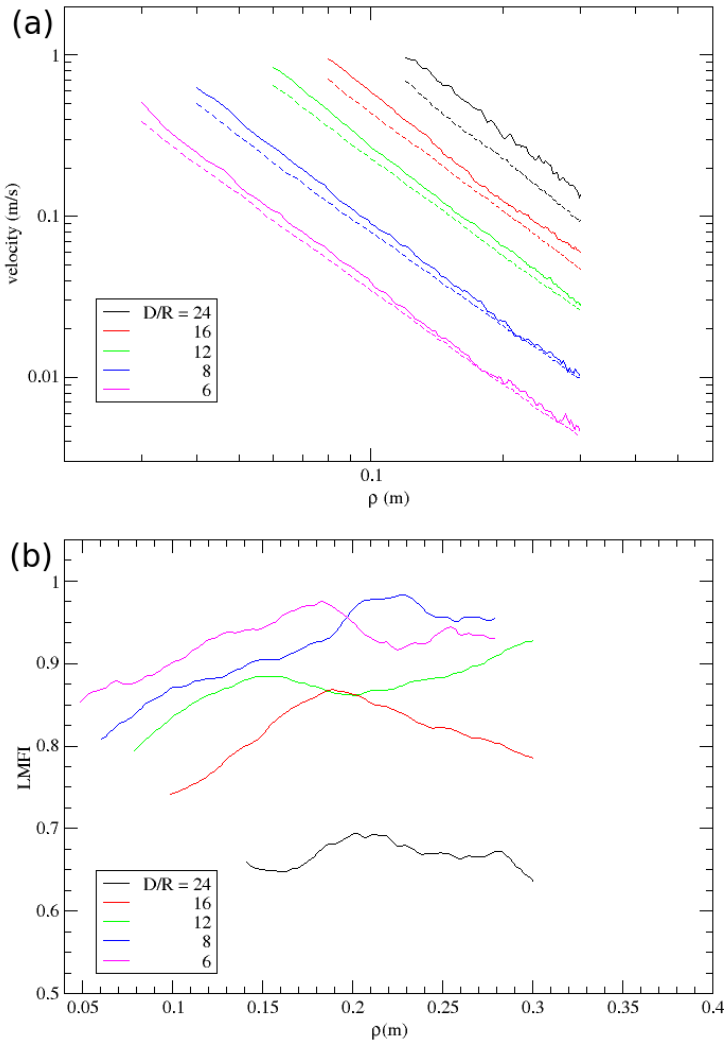

Figure 14: Velocity profiles for center (solid line) and wall (dashed line) velocities in log-log scale (a) and Local Mass Flow Index (b) are plotted for different orifice diameters, $\Theta = 60°$ and $k_t = 100$ N/m. The profiles are power laws, but slightly different inclinations between v_{w} and v_{c} can be observed for some cases which causes the I_{LMF} to rise. The larger the orifice diameter the larger is the gap between center and wall velocities and consequently the lower is the I_{LMF}. We estimate values of I_{MF} between 0.71 and 0.77 for these cases.

5.3 The Influence of the Spring Constant of the Static Friction Force

We present in this section a comparison between the data presented previously and those from similar simulations where the spring constant in the static friction force law was $k_t = 10^5$ N/m instead of 100 N/m. This new value is closer to real materials and avoids the possibility of non physical behavior and numerical instabilities as discussed in Section 4.3.

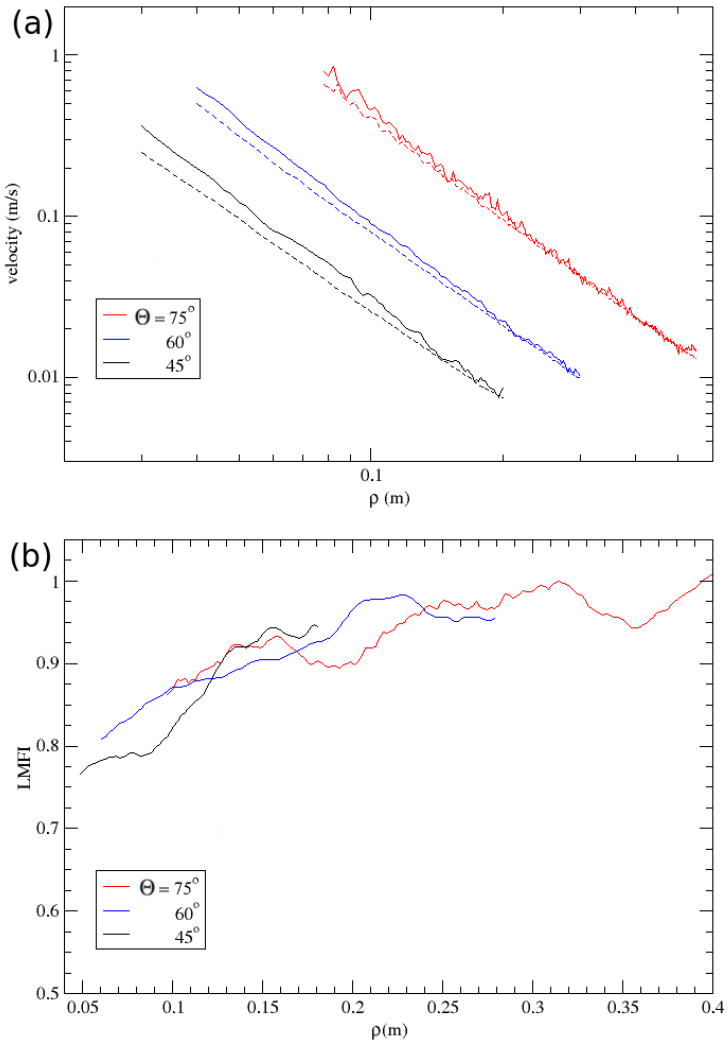

Figure 15: Velocity profiles for center (solid line) and wall (dashed line) velocities in log-log scale (a) and Local Mass Flow Index (b) are plotted for different hopper angles, $D = 8R$ and $k_t = 100$ N/m. As in figure 14a, power law behavior is observed for the velocity profiles. Here, the differences between the center and wall velocities close to the outlet are larger for smaller θ, however, the difference vanishes for large ρ in all cases. This is represented in panel (b) by the low values of I_{LMF} for small ρ that then rise up to values close to unity. We estimate values of I_{MF} between 0.68 and 0.84 for these cases.

The analyses are identical to those performed in the last section, with the spatial averages taken over a square cell of sides equals to 0.006 m on the $z-r$ plane and spanning along the azimuthal coordinate, θ. Average on time was computed over typically 1000 snapshots taken every 0.005 s, that is, every 5000 time steps.

The behavior observed in the velocity profiles for $k_t = 100$ N/m, as shown in Figure 14, was maintained for the simulations with a different value for k_t. That is, for $k_t = 10^5$ N/m, the velocity along the walls of the hopper, v_w, as well as that along the central axis of the cone, v_c, are approximate power laws in function of the distance from the vertex

of the hopper, ρ. That can be seen in Figure 16a. In Figure 16b, we show the data for simulations of same system geometry, but the value of k_t is that of the last section. The reader should note that the graphs are qualitatively identical.

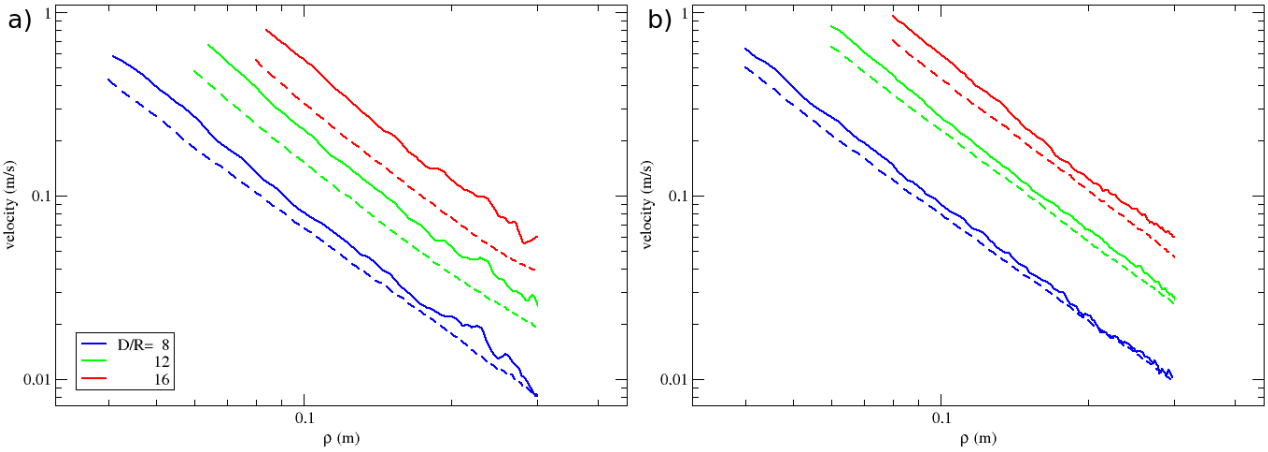

Figure 16: Velocity profiles are plotted in log-log scale along the center, v_c, (solid line) and along the walls, v_w, (dashed line) of a conical hopper with an angle of 60° with the horizontal plane. a) $k_t = 10^5$ N/m; b) $k_t = 100$ N/m.

Differences arise when the pair of profiles (v_w e v_c) for each orifice diameter are compared separately. In Figure 17 it is possible to see that v_c has changed very little, on the other hand, v_w has decreased in absolute values considerably with the change in k_t. That behavior is not surprising, as k_t is a parameter of the tangential force in the static regime, state of most of the grains in contact with the walls. For those grains, the movement is much slower and their contacts last for longer than those of grains along the center of the hopper, where contacts form and break very often. Contacts that last for short periods of time cannot build long spring displacements, ζ, as part of the tangential force and therefore the value of parameter k_t which multiplies that displacement is less relevant.

As we discussed before, the Mass Flow Index, I_{MF}, may be sensible to the choices for the geometry of the averaging region. In this light we have proposed the Local Mass Flow Index, a profile in function of the distance from the hopper vertex . We present the graph for $I_{\mathrm{LMF}}(\rho)$ in Figure 18a for the simulations with $k_t = 10^5$ N/m. Note that values for the index vary from 0.55 up to 1.0. As discussed before, values of the index close to the unity mean the velocities along center and along the walls at the same distance from the vertex of the hopper are close in magnitude. Small values for I_{LMF} represent situations where the velocities along the center are much larger than those along the walls, an indication of stagnation zones, and, henceforth, indication of funnel flow regime

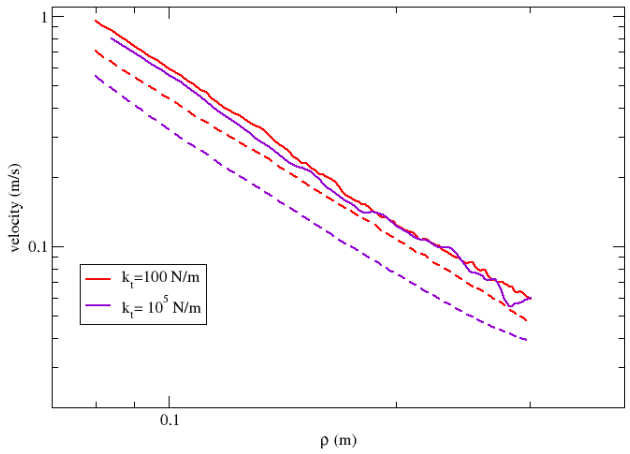

Figure 17: The central velocity profiles, v_c, (solid lines) and wall velocity profiles, v_w, (dashed lines) are compared for simulations with either $k_t = 100$ N/m or $k_t = 10^5$ N/m for a conical hopper with 60° angle with the horizontal plane, in log-log scale.

as well. The observed values, even though they are comparatively small for the simulation with orifice of diameter $D = 16R$, can not to be considered in funnel flow regime. In the literature [23, 30] it is usual to consider in that regime when $I_{\mathrm{MF}} < 0.3$.

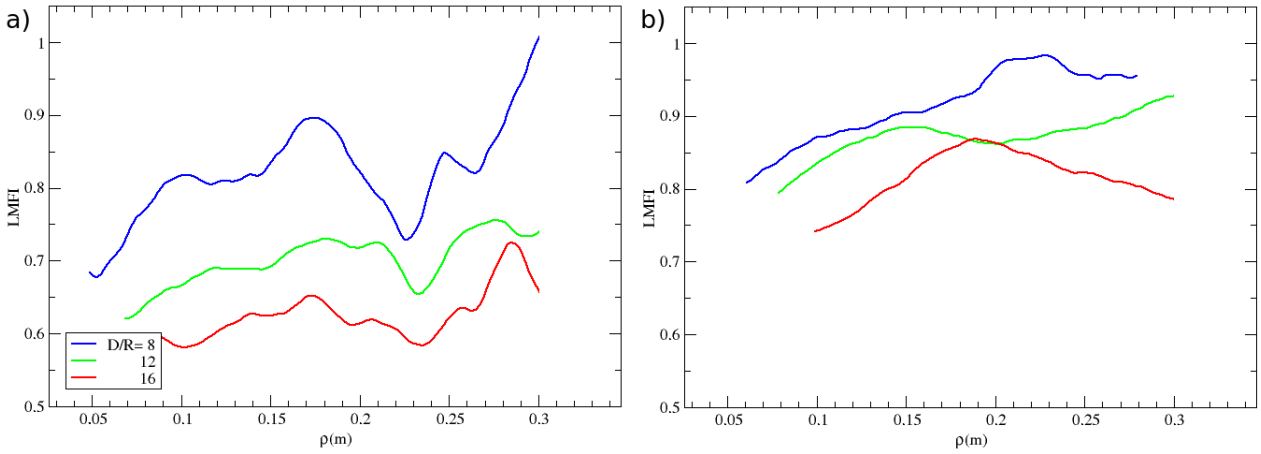

Figure 18: Local mass flow index profiles, I_{LMF}, are plotted for a conical hopper with 60° angle with the horizontal plane. a) $k_t = 10^5$ N/m; b) $k_t = 100$ N/m.

Note in Figure 18b that larger values of I_{LMF} for each orifice size are found for simulations with $k_t = 100$ N/m as compared to those for $k_t = 10^5$ N/m, as previously discussed. In general, the index varies from 0.6 up to 1.0. This effect corresponds to the difference between the velocities along the walls for each choice of values for the tangential force parameter k_t. The influence of the change in the parameter, and therefore in the tangential force, is more pronounced in the regions closer to the walls than to the central axis of the hopper. Hence, as the velocities along the central axis are approximately the same for the different values of k_t while the values for the velocities along the wall are

much smaller for the largest value of k_t, we perceive a decrease in the index values as it is computed by the ratio between the wall and central velocities. It is possible to observe a growth in the index for increasing ρ for the smaller value of k_t, Figure 18b. However, this effect is not so clear for Figure 18a, where k_t is larger, as fluctuations are much stronger.

These results do not contradict the conclusions from the last section and from our paper [89]. The differences observed between the simulations with different values of k_t can be understood by the direct influence of this parameter in the dynamics of the system. This study on k_t was motivated by a discussion during the revision of the paper as one of the referees argued that value we used, at first, $k_t = 100$ N/m, is not within the range comparable to real materials, and more importantly, it could even lead to unphysical behavior and numerical instabilities in the grounds discussed by Schaeffer et al. [84]. However, those issues were not observed in our simulations. We believe that by using a nonlinear normal force the spurious effects discussed in their work were avoided.

In summary, our results show that the Local Mass Flow Index profile varies along ρ for many hopper angles and opening widths. This dependence raises concerns over the characterization based solely on the Mass Flow Index, where this information is lost. Nevertheless, the analysis of the I_{LMF} profiles was shown to be an appropriate tool to describe the more subtle aspects of the flow. Although our simulations were limited to mass flow regime, we expect that more distinctive features will be observed for discharges in the funnel flow regime, which is part of our current investigations.

6 Force on the Walls

6.1 Time Series Fourier Spectrum

The time series of flow characteristics in granular dynamics has been the subject of many studies [17, 19, 20, 44, 45, 46, 91, 92]. It has been noted that the fluctuations of many of such characteristics show an interesting feature: $1/f^{\alpha}$ spectra. Signals that exhibit this type of fluctuation are ubiquitous in science and are often related to self organization mechanism [74, 93]. In granular materials, the power law in the power spectrum has been observed not only in discharges, but also in slowly shearing systems [92]. Baxter *et al.* [19, 20] observed a $1/f^{\alpha}$ noise experimentally in the difference between the stresses exerted on two positions on the walls of a hopper. They intended to confirm the characteristic time scale for such a system as predicted by continuum models, however, no time scales can be defined for this type of fluctuation. Additionally, they discussed the relations of this behavior to the spectra of fractional Brownian motion and obtained the Hurst exponent of the time series [94, 95]. The exponent α showed a relation with the Hurst exponent, H, through the equation

$$\alpha = 2H + 1 \ , \tag{6.1}$$

as predicted theoretically. From the Hurst exponent, or from α as they are related by the equation above, they could obtain also the fractal dimension of the time series, D_f, as

$$D_f = 2 - H \ . \tag{6.2}$$

In their work, Baxter and collaborators observed values for α varying from 1.3 up to 2.3 for different types of grains and different flow rates. Finer grains showed smaller α and Hurst exponents, and they noticed that the exponents dropped with increasing flow rates, however, both the dependences were not very strong.

Ristow and Herrmann [17] studied the fluctuations on the pressure acting on the walls of two-dimensional hopper-bottom silos via computational simulations. They studied

varied hopper opening angles, starting from steep hoppers to an almost horizontal bottom silo, as can be seen in Figure 19. They observed the latter is a discharge in the funnel flow regime as it presents stagnation zones, absent in the former situation. In the figure reproduced here, the stagnation zones are observed in panel (a) as the "S" shaped contour lines reach down to the outlet. On the other hand, in panel (b), such lines and their slopes are limited by the walls of the hopper, thus they regard this case as a "mass flow" (no stagnation zones), and the first case as "funnel flow".

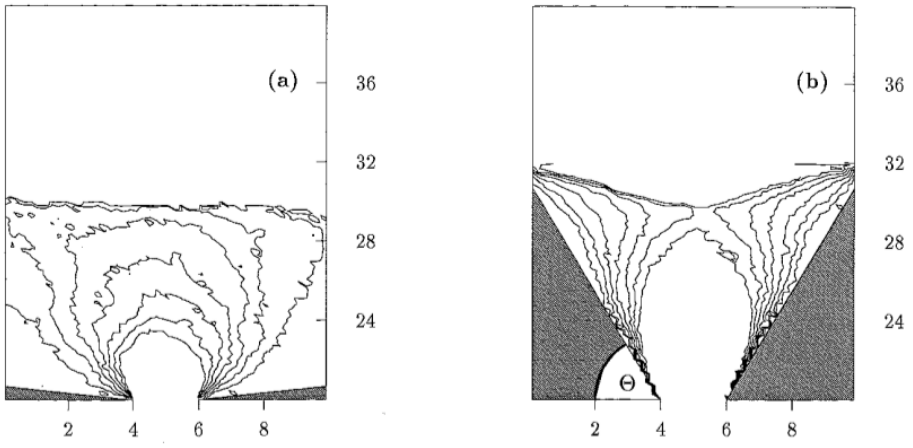

Figure 19: Contours of equal kinetic energy in an outflowing hopper during outflow for (a) an angle of $\Theta = 10°$ and (b) $\Theta = 70°$. The axes are measured in cm. Extracted from [17].

They also observed that the fluctuations presented the power law spectra as in the aforementioned experiments. Moreover, they observed a dependence of α on the angle of the walls of the hopper, and therefore, with flow regime, what is shown in Figure 20. For increasingly steep hopper walls the value of the exponent diminishes until the spectra becomes white noise which means that there is no significant correlation in the time series, as seen in Figure 20b. On the other hand, more open hoppers showed power law spectra with exponents reaching values close to 2. Considering that the exponent on the power spectrum of a fluctuation is related to correlations in the time series, as discussed, they propose that it is exactly the stagnation zones that are responsible for the power law spectra, as they act as "noise transformers", as through their contact network the originally uncorrelated collisions of moving grains becomes correlated.

We contribute to the discussion analyzing the dependence of the power spectra of the pressure on the hopper upon the distance from the orifice. None of the aforementioned works have explored what is the influence of the position where the pressure is taken for the construction of the time series.

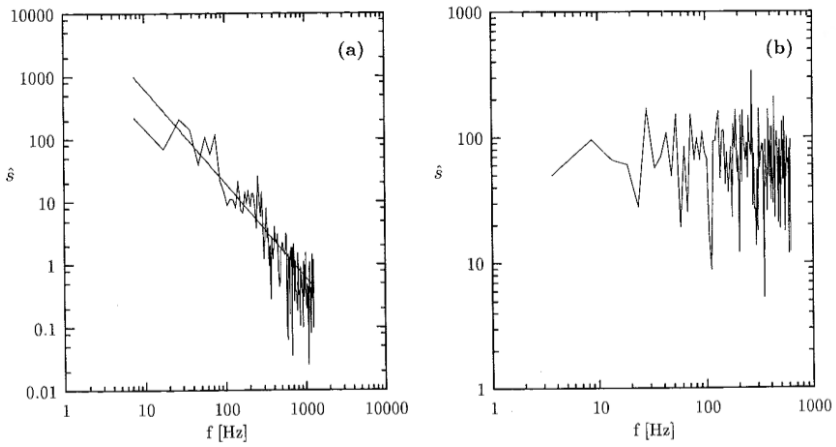

Figure 20: Log-log plot of the power spectrum $\hat{s}$ of the stress measured in arbitrary units for different angles Θ of the hopper measured 11 particle diameters above the orifice (a) $\Theta = 40°$ and (b) $\Theta = 75°$. The straight line in panel (a) corresponds to an exponent of $\alpha = 1.80$. Figure extracted from [17].

The time series is obtained taking the normal forces acting on square bins of the wall at time intervals of 0.005 s (5×10^3 time steps). Those bins are 0.006 m wide, so that only one contact is possible at a time. It is clear from the time series, as seen in Figure 21, that different behavior occur for different positions in the hopper, which are denoted by the distance from the orifice, $\rho^* = \rho - D/(2\cos\Theta)$, where ρ is the distance from the vertex of the hopper cone, as defined in Figure 11.

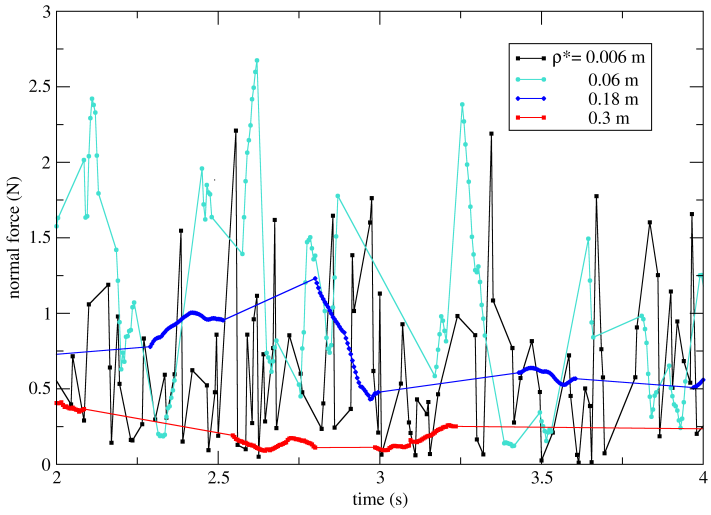

Figure 21: Normal force time series is plotted for different positions in the hopper. Conical hopper with 60° angle with the horizontal plane and orifice diameter $D = 12R$, $k_t = 10^5$ N/m.

The fluctuations on the time series are much stronger closer to the orifice than for larger ρ^*. On the upper regions we notice long periods of no contact for each bin of

the hopper wall followed by periods of slowly varying forces. This can be understood as an effect of quasi-stagnant zones, where the grains are in long lasting approximately crystallized packings, traveling down the hopper. Contrastingly, close to the outlet, only short periods of no contact occur. However, we can safely assume that consecutive entries of the normal force time series are rarely from the contact of the same grain as they travel fast. In fact, from Figure 16 we notice that close to the outlet velocities are typically around 1 m/s, as the interval of time between the observations on the force is 0.005 s, and therefore each grain travels a distance of approximately 0.005 m. That distance is roughly the width of the bin where the force is observed. We do not try to avoid such irregularities in the acquired data as it is an important feature of the dynamics of the system.

The Fourier Transform of the time series was then obtained using Grace® software [96] built-in function Discrete Fourier Transform and presented in Figure 22. For convenience of the remaining analysis we take the logarithm of each axis. The results are similar to those obtained by Ristow and Herrmann [17], however, in the present case, both curves are for the same simulation on different positions. In their work the two behaviors were observed for the same distance from the outlet, but different opening angles. As the power spectrum corresponds to the square of the Fourier spectrum, α is twice the exponent obtained from the latter. The white noise spectrum for the time series close to the orifice indicates uncorrelated collisions as discussed before. On the other hand, at larger distances away from the outlet, the force on the walls shows a power law spectrum with $\alpha = 1.86$.

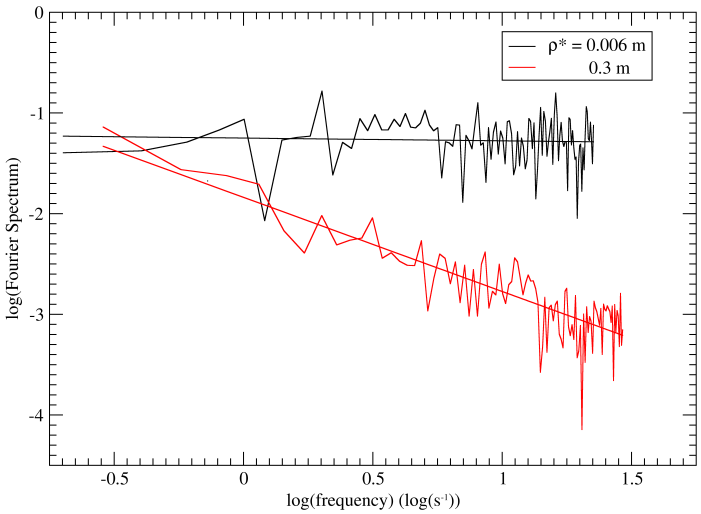

Figure 22: Logarithm of the Fourier Transform of time series shown in Figure 21 plotted as a function of the logarithm of the frequency. Straight lines are for linear regressions.

The dependence of α on the distance from the orifice can be investigated further by

repeating the procedure described so far for the entire extent of the hopper. Moreover, we apply the procedure for four choices of the azimuthal angle, $\theta = 0$, $\pi/2$, π, and $3\pi/2$, and take their average, Figure 23.

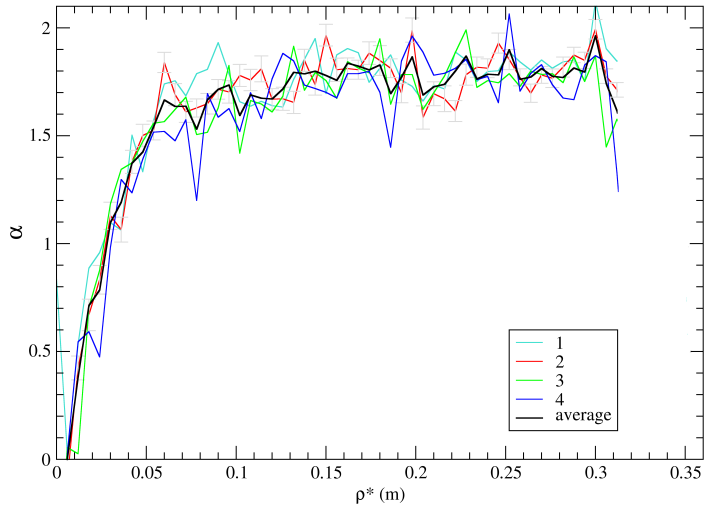

Figure 23: Exponent α plotted in function of ρ^*, the distance from the orifice. Showing curves for different choices of the azimuthal angle, $\theta = 0$, $\pi/2$, π, and $3\pi/2$, marked 1 to 4, and their average.

Despite the fluctuations, a clear trend is observed. The exponent rises from $\alpha = 0$ close to the outlet to a plateau at approximately $\alpha = 1.8$. An abrupt drop on α was observed for very large ρ^* which is due to surface and reinsertion effects and it was omitted here. The plateau represents a bulk behavior that is clearly separable from the behavior close to the outlet. The value, $\alpha \simeq 1.8$, is consistent with the observations by Ristow and Herrmann for funnel flow regime, however, they observed the exponent only for the most open hoppers and at an 11 diameter distance from the orifice, which corresponds to $\rho^* = 0.055$ m in our case. In Figure 24, we present the curves for the exponent α for different orifice sizes. In all cases, after the average over 4 different azimuthal directions, as discussed, we also perform a running average over 5 points to suppress the fluctuations, whereas the most important features are maintained. We believe that the fluctuations should be less pronounced if longer simulations were performed, which is not practical at the time due to the long periods necessary for the computations. Longer time series would lead to a wider spectrum and a more accurate assessment of the exponent.

From Figure 24, it is clear that the size of the orifice influences only the width of the growth zone for α, but not its saturation value, $\alpha \simeq 1.8$. In fact, as it is shown in the inset, the curves roughly collapse if the horizontal axis is scaled by the diameter of the orifice in units of the average radii of the grains. This result can be explained by the fact

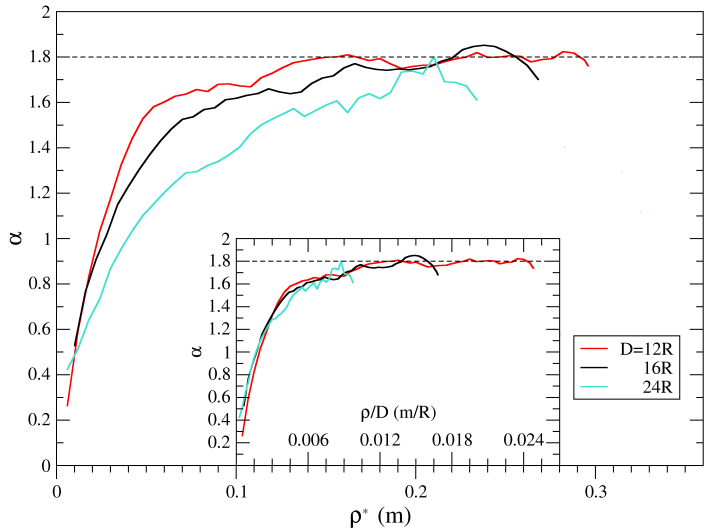

Figure 24: Exponent α plotted as function of ρ^*, the distance from the orifice for different diameters of the orifice. Running averages over 5 points are taken. In the inset, the same plot is shown with the abscissa rescaled as ρ/D and showing the collapse of the curves.

that the ratio D/R is the main characteristic length scale of the system. Hoppers with the same opening angle and spatial coordinates scaled by that ratio are indistinguishable.

The spectra exponent α is therefore an useful measure of the structure of the granular material close to the walls of a hopper. In a region where the time series of the forces acting on the wall are white noise or presents α around, or smaller, than unity, it is expected that independent collisions dominate the grain-wall interactions. On the other hand, if α is larger, typically close to 2, clogs of grains arranged in a reasonably stable configuration transform the independent kicks of fast moving grains into a correlated signal. The analysis of α as a function of the position for different geometries of the container is among the inquires we intend to pursue in the future. The results may lead to interesting characterization of the flow regime with the advantage of being fairly easy to implement in experiments and commercial applications by the use of stress transducers on the inner walls of the container.

6.2 Force Distribution

We have studied in the last section the temporal fluctuations of the forces acting on the walls of a hopper. In the present section, we take a more traditional approach to assess the statistical properties of such forces by studying their probability distribution for different hopper geometries and at different regions in the hopper.

It has been noted for biaxially compressed bi-dimensional granular systems that the functional behavior of the probability density functions (PDF) of the normal force between grains depends on the packing fraction and the friction coefficient between the grains [97]. In fact, Kramar *et al.* have shown that Gaussian-like distributions occur for more tightly packed configurations, that is, large packing fractions, whereas for configurations where the grains are looser and large force chains are present the normal force distribution has the exponential tails recurrent in various experiments and simulations of grains [98, 99, 97]. Also by compression of bi-dimensional systems containing either granular materials or emulsions, Zhang and Makse [100] showed similar results for the PDFs shapes and its relation to the structure of the material which was thoroughly studied. They concluded that at low pressures there are very large forces in the packings and the forces are distributed heterogeneously. That is, there are few and well distributed force chains carrying the largest forces and the material is dilated. The tails of the PDFs that represent the probability of force much larger than its mean are roughly exponential, however, with increasing pressure, they bend down and transform into Gaussian-like curves. Thus, it indicates that the very large forces (in comparison with the average force) are disappearing and that the package is becoming homogeneous with contacts having more probably forces similar to their average. The latter conclusion is confirmed by the authors by the calculation of the participation number, a measure of the structure of the force network that will not be discussed here.

The probability density function for the normal forces exerted by the granular material on the walls of the hopper during discharge is the subject of this section. The natural first step is to study the distribution of the forces on the walls of the full extent of the hopper, as shown for various systems in Figure 25. Firstly, we have computed $\bar{F}_n = F_n/\langle F_n \rangle$, so that the force is normalized by its average. Then a normalized frequency count is calculated using the built-in function in Grace Software [96]. A very complex behavior is observed for forces around the average force, $\bar{F} \simeq 1$, which depends on the orifice size. Nevertheless, exponential tails are observed for larger forces, typically larger than four times the average force. As discussed before, this is an indication of heterogeneous transmission of stress through sparse force chains and is an issue of practical concern in hopper design.

We investigate further this result by the analysis of the PDFs of the normalized normal force at various regions of the conical hopper. We slice the cone at intervals of 0.006 m, as measured along the wall, therefore along ρ^* the distance from the orifice, and take the distribution of forces at each of the resulting rings. As this procedure generates a large

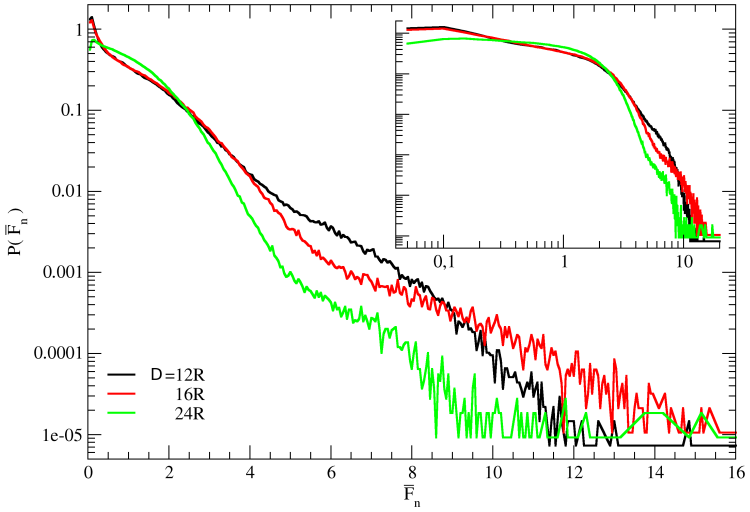

Figure 25: Probability density functions for the normal forces on the walls of the hopper normalized by its average plotted for various simulations.

number of curves, typically around 50, we will present only a few indicating when similar behavior is omitted. We will analyze two of the situations presented in Figure 25 and discuss what the distribution reveals about the flow and the structure of the granular material in the hopper.

The distributions are represented by ρ^*, the distance from the outlet to the beginning of the region where they are computed. Therefore, the region denoted by $\rho^* = 0$ m is the ring of the wall starting from a distance 0 m from the outlet and extending until 0.006 m further up along the wall of the hopper. Note that it is the distance from the orifice and not from the vertex of the cone. The average forces for each of those regions are also different, as can be observed in Figure 26. The average force rises from the top of the hopper down until a maximum and then it drops due to the orifice.

The PDFs of the normal force for various regions of the hopper with orifice with diameter $D = 12R$ are presented in Figure 27. It is possible to observe in panel (a), that for the first region, $\rho^* = 0$ m, the PDF behaves roughly as an exponential function, however, for the following sections the tails of the distribution bends down and its tail rapidly becomes Gaussian-like. The system maintains the latter behavior for a long region of the hopper. The curves for regions between 0.018 m until 0.168 m are visually indistinguishable. The approximately Gaussian tail bends back to an exponential tail in the regions closer to the open surfaces on the top of the granular material, as it is seen in Figure 27(b).

A very similar behavior is observed for larger orifice diameter, $D = 24R$, in Figure 28.

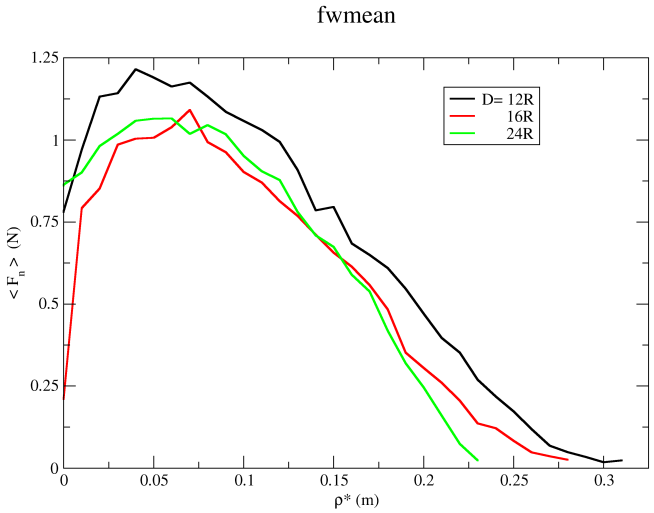

Figure 26: Average force plotted for various positions and orifice diameters.

The Gaussian-like tail of the PDFs is maintained at most of the extent of the hopper, in fact the heavier tail for the PDF immediately above the outlet is much more subtle than for the former system, as it is not clearly exponential. The region close to the free surface of the granular material presents the exponential tails for distances to the orifice around 0.246 m.

Based on the interpretations of the shape of the PDFs curves discussed in the beginning of this section, we can infer much of the structure of the grains force network. As we have computed PDFs for only the forces on the walls of the hopper, all conclusions are for the grains in contact or very close to the walls. Figure 27 and Figure 28 show that for a large region of the hopper the tails of the PDFs are approximately Gaussian, and therefore the grains (close to the walls) must be tightly packed with small probability of extreme events. However, for those cases, the granular material in the region close to the free surface is probably in a more dilated configuration, dominated by sparse force chains, as the distribution of forces present exponential tails.

The trajectories of selected grains in the hopper for both the orifice sizes discussed before are shown in Figure 29. This figure was produced by taking the grains in a slice one grain diameter wide across the diameter of the hopper and plotting lines for each of them connecting the positions of their center for an interval of 0.15 s, or 1.5×10^5 time steps. In panel (a), we observe that, for the smaller orifice, there is almost no movement of the grains near the walls of the hopper for ρ^* larger than 0.1 m as their trajectories are point-like or very short dashes, also we note that those grains are organized in an

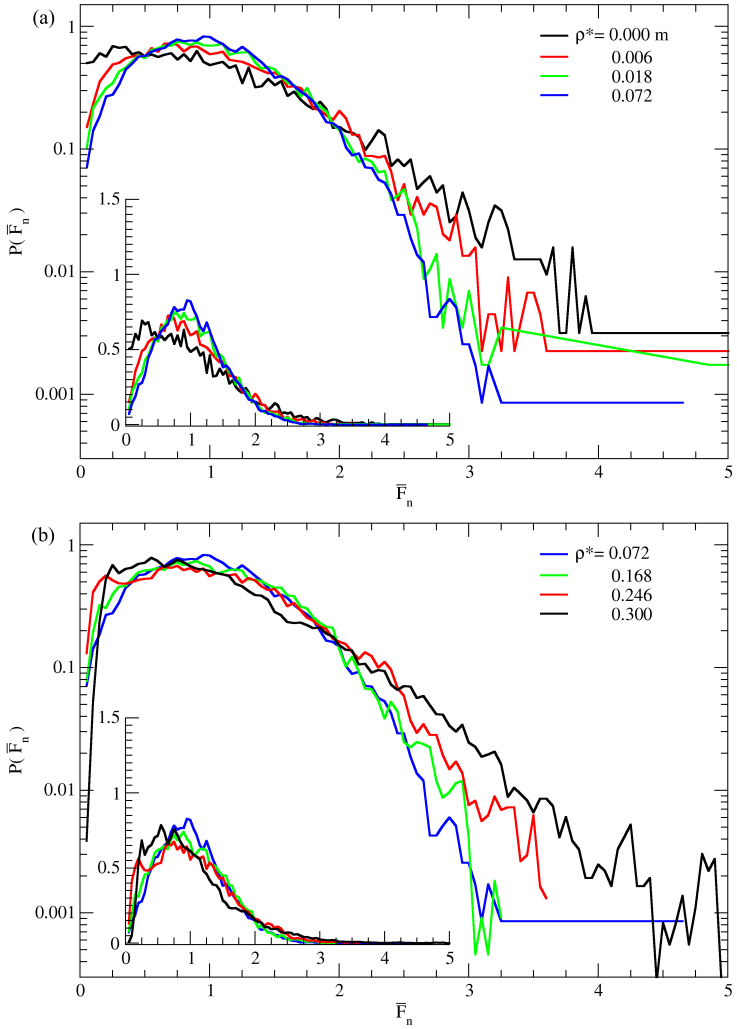

Figure 27: Probability Density Functions for the normal forces on the walls of the hopper normalized by its average plotted for orifice diameter $12R$ at various regions on the hopper. Note that the order of color in function of ρ^* is inverted from panel (a) to panel (b).

almost crystallized structure. In panel (b), we can see that, even though the trajectories are much longer for this larger orifice size, those close to the wall are roughly parallel to it. These observations are in accordance to those on the PDFs of the normal forces on the walls of the hopper, that is, the idea of an organized cluster of grains streaming through the hopper.

A more detailed study of the relation between the structure of the flowing granular material and the force on the walls is a prospective theme of research, just as experimental validation of the observations. The force network for the systems we analyzed are an important part of the large collection of data that is available, as shown in Figure 30, which was obtained for the same slices of the trajectories in Figure 29. The study of the topology of the force network in different regions of the hopper may bring new insights

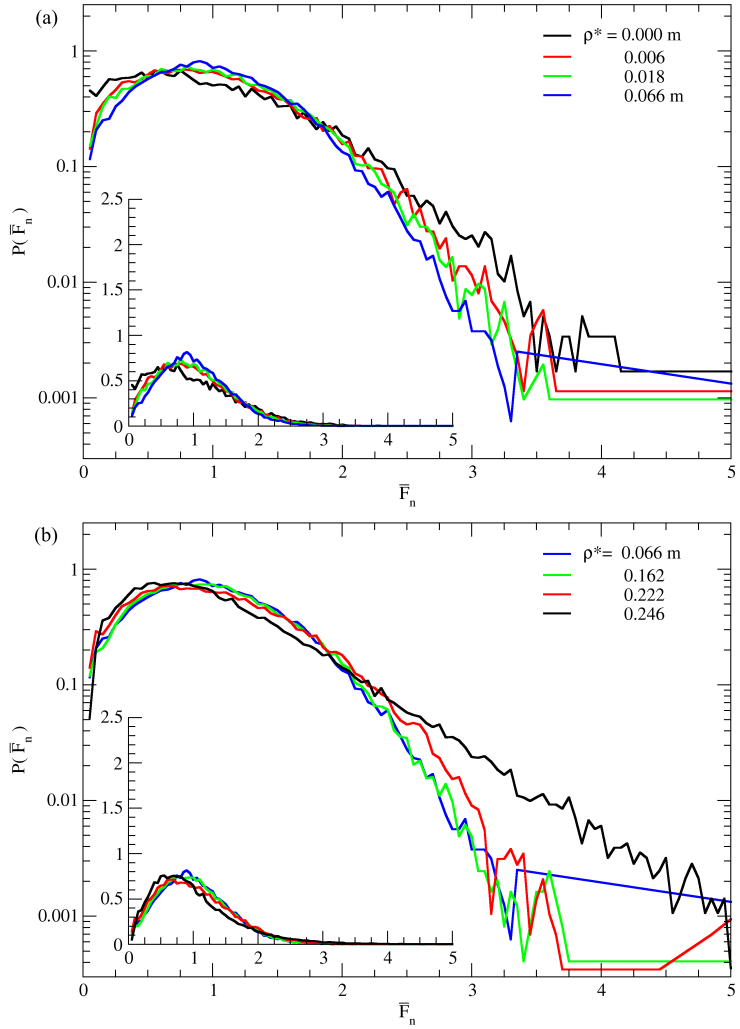

Figure 28: Probability Density Functions for the normal forces on the walls of the hopper normalized by its average plotted for orifice diameter $24R$ at various regions on the hopper. Note that the order of color in function of ρ^* is inverted from panel (a) to panel (b).

of the structure of grains and its relation to the distribution and power spectrum of the force on the walls of the hopper.

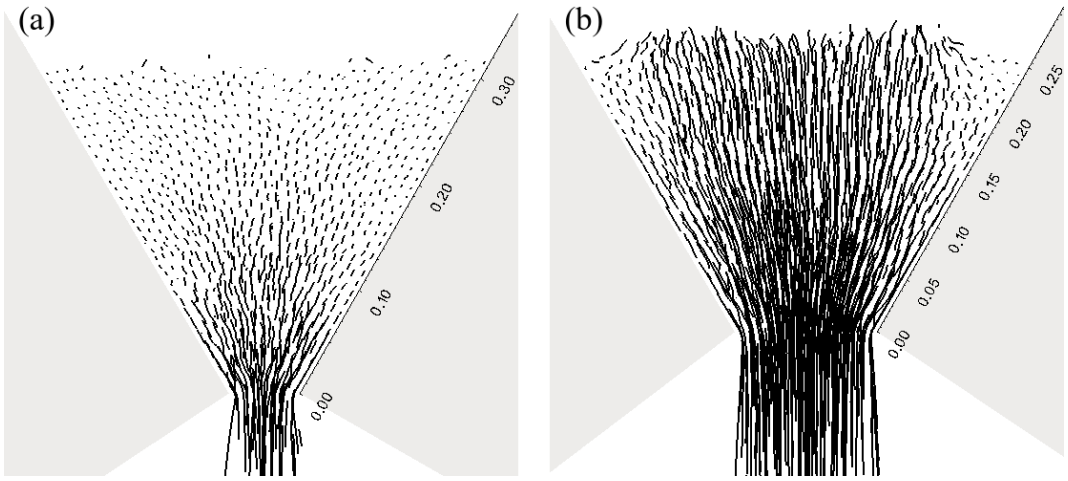

Figure 29: Trajectories of the grains in a slice $2R$ wide along the diameter of the hopper plotted for an interval of 0.15 s. (a) $D = 12R$, (b) $D = 24R$.

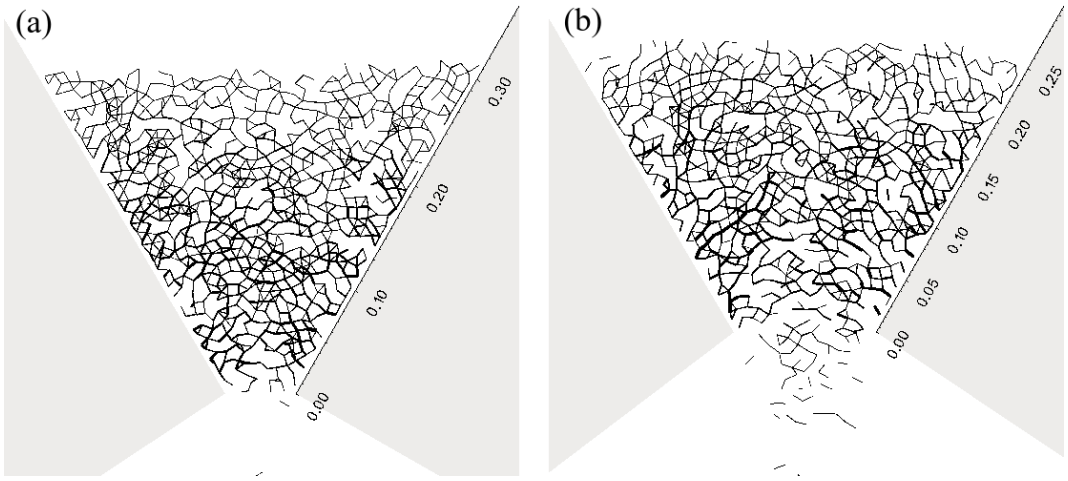

Figure 30: Network of normal forces between grains in a slice $2R$ wide aligned along the diameter of the hopper is shown. Each line connects the centers of a pair of grains in contact and its width is proportional to the normal force between them. (a) $D = 12R$, (b) $D = 24R$. Note that the image shows a projection onto the longitudinal plane and most of the lines are not parallel to the plane or to one another.

7 Conclusions and Perspectives

We have studied the flow of spherical grains through conical hoppers by computational simulations. The flow of grains through an aperture has been subject of great academic and industrial interest for centuries, and it is still an active field of research. The Discrete Element Method simulation was the chosen approach, for it is a powerful tool present in a significant portion of the literature of granular dynamics, and presenting the advantage of easy access to a large collection of physical quantities. Our analyses were focused on statistical characteristics of the flow and their spatial resolution, in particular, the dependence on the distance from the outlet. Different orifice diameters were employed and for some studies the influence of the opening angle of the hopper was also investigated. The quantities analyzed were the average velocity of the grains, the time series and the distribution of the forces on the hopper wall.

The velocity profiles along the axis of the hopper and close to the walls were studied, as well as their ratio, the I_{LMF} profile. Both velocity profiles show approximately a power law dependence with the distance from the vertex of the hopper for the considered cases. For the simulations with $k_t = 100$m/s and hoppers with large orifice widths, there is an upshift of the velocity profile along the center of the hopper as compared to that close to the walls, but the slopes are roughly the same. This is accompanied by a I_{LMF} that fluctuates around a certain value that can be as low as 0.65 for the largest orifice width analyzed. On the other hand, for small outlets, the difference between the profiles decreases with the distance from the opening. This decrease is clearer when the angle of the hopper is changed. The smaller the angle of the walls of the hopper with the horizontal plane, the larger the slope of the central velocity profile compared to the wall velocity profile. In all those cases, the velocity profiles do not cross each other, so that, for a distance farther from the orifice, the difference of the slopes becomes negligible. This decrease in difference between the velocity profiles is seen as an increase of I_{LMF}. The I_{LMF} stabilizes with values close to one in the regions where the velocity profiles collapse. Qualitatively similar behavior is observed for $k_t = 10^5$m/s, however,the I_{LMF}

values are smaller when compared to results for equivalent orifice sizes and smaller k_t. This quantitative difference is attributed to the direct physical effect of the parameter, as larger frictional forces will appear on the regions close to the wall slowing down grains. However, the grains close to the hopper axis will be less affected, as there the contacts typically last less.

The temporal correlations of the forces acting on the wall of the hopper have been studied through the power spectra of their time series. Due to these correlations, $1/f^{\alpha}$ spectra can be observed and α is also an indicator of the presence of stagnation zones in the flow [17]. We obtained this exponent for different distances from the outlet in the hopper. For small distances, α is zero, but as they increase it rises until a plateau is reached. The value at the plateau seems to be universal among different orifice sizes and the growth rate is inversely proportional to the orifice diameter. This novel result shows that α varies within the hopper consistently and even though there are no stagnation zones, correlated signals are observed.

The Probability Density Function (PDF) of normalized forces exerted by grains on areas of the wall obtained at different distances from the orifice present either exponential or Gaussian-like tails. For positions immediately close to the outlet or close to the free surface of the granular material, exponential tails are observed. The distributions with Gaussian-like tails are observed for the remaining positions between those extremes. These distributions exhibit similar behavior to what is seen in confined static packings [98, 99, 97, 100]. In accordance with the conclusions of these works, we believe that the Gaussian-like tails are indication of a close-packing structure with fast dropping probability for forces increasingly larger than the mean. Contrastingly, the exponential tails are indicative of a more dilated structure with the presence of force chains, resulting in a more heterogeneous distribution of the forces and a larger probability of extreme events.

These results provide a deep understanding of the flow of the granular material. The Local Mass Flow Index show there is a significant difference between the velocity at the center and at the wall of the hopper, which is an indication of funnel flow. However, no stagnation zones are observed. On the other hand, both the analyses on the forces on the walls, the time series spectra and the PDFs, yield outcome analogous to that expected for stagnant structured packings. These results are compatible with the scenario of slowly moving structured zones where no statistical change is observable, at least for the time scale of the simulation. In this scenario, the effects on the normal forces on the wall of the hopper would be equivalent to those of stagnation zones, even though the velocity profile

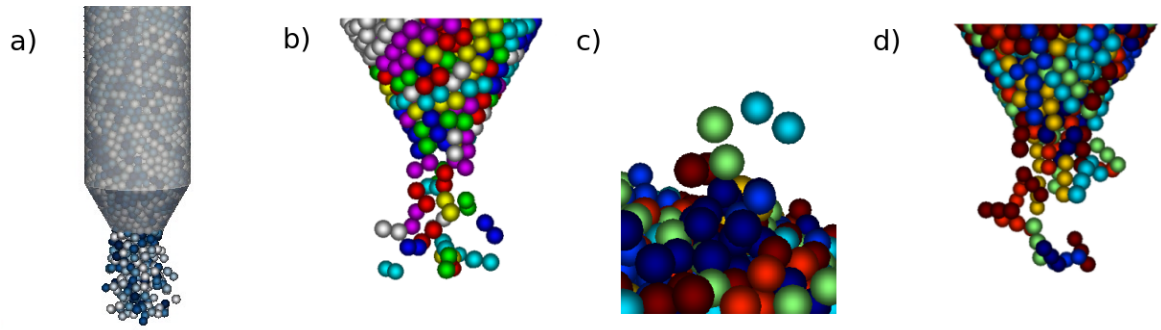

Figure 31: Snapshots of preliminary simulations of different container and grains geometries are presented. a) Silo container geometry consists of a conical hopper bottom and a cylindrical bin; b) grain composed of two spheres in contact; c) grain composed of two separated spheres; d) grain composed by three spheres aligned and in contact.

would not vanish. This conclusion indicates that the merely analyzing of the forces on the wall of the hopper may not be enough to characterize the flow regime within.

Many other questions can be pursued from the data gathered from the simulations and many more simulations can be performed using the same basic code. Among our more immediate plans to continue the study of granular discharges we cite three. As indicated at the end of Chapter 6 and illustrated by Figure 30, the characterization of structure measures using the contact network that is already available from the data can serve as a complement to the analyses presented here and it can, possibly, confirm and extend the understanding we have of the system. Additionally, we intend to repeat the analyses for a hopper-bottomed cylindrical silo, as seen in Figure 31a, where a fully developed funnel flow discharge, presenting stagnation zones can be obtained. Initial tests have been performed. However, improvements are necessary before the simulations can provide reliable data. At last, another interest of ours since the beginning of the project is the study of the influence of the grains aspect ratio on the flow characteristics. Our simulation code was written considering grains composed of multiple spheres that are rigidly maintained at regular distances, as shown in Figure 31b-d. The construction of different geometries of the grain by this procedure has many advantages such as a high computational efficiency, simple coding, possibility of arbitrarily long and complex composites and easy interactions in mixtures of different types of composites.

References

[1] Herrmann, HJ: *Grains of understanding*. Physics world, 10(11):31–34, 1997.

[2] Jaeger, HM, SR Nagel e RP Behringer: *The physics of granular materials*. Physics today, 49:32–39, 1996.

[3] Jaeger, HM, SR Nagel e RP Behringer: *Granular solids, liquids, and gases*. Rev. Mod. Phys., 68:1259–1273, Oct 1996. `https://link.aps.org/doi/10.1103/RevModPhys.68.1259`.

[4] Campbell, CS: *Granular material flows–an overview*. Powder Technology, 162(3):208–229, 2006.

[5] Duran, J: *Sands, powders, and grains*, volume 12. Springer, New York, 2000.

[6] Mehta, A: *Granular matter: An interdisciplinary approach*. Springer, 1994.

[7] Ketterhagen, WR, MT am Ende e BC Hancock: *Process modeling in the pharmaceutical industry using the discrete element method*. Journal of Pharmaceutical Sciences, 98(2):442–470, 2009, ISSN 1520-6017. `http://dx.doi.org/10.1002/jps.21466`.

[8] Cleary, PW e ML Sawley: *DEM modelling of industrial granular flows: 3D case studies and the effect of particle shape on hopper discharge*. Applied Mathematical Modelling, 26(2):89–111, 2002.

[9] `http://www.iea.org/newsroom/energysnapshots/world-total-coal-production-1971-2016.html`.

[10] Zuriguel, I: *Clogging of granular materials in bottlenecks*. Papers in Physics, 6:060014, 2014.

[11] Janda, A, I Zuriguel, A Garcimartín, LA Pugnaloni e D Maza: *Jamming and critical outlet size in the discharge of a two-dimensional silo*. EPL (Europhysics Letters), 84(4):44002, 2008. `http://stacks.iop.org/0295-5075/84/i=4/a=44002`.

[12] Magalhães, CFM, JG Moreira e APF Atman: *Catastrophic regime in the discharge of a granular pile*. Physical Review E, 82(5):051303, 2010.

[13] Magalhães, CFM, APF Atman, G Combe e JG Moreira: *Jamming transition in a two-dimensional open granular pile with rolling resistance*. Papers in Physics, 6(0), 2014.

[14] Magalhães, CFM, JG Moreira e APF Atman: *Segregation in arch formation*. The European Physical Journal E: Soft Matter and Biological Physics, 35(5):1–5, 2012.

[15] Ristow, G e HJ Herrmann: *Density patterns in two-dimensional hoppers*. Phys. Rev. E, 50(R5), 1994.

[16] Artega, P e U Tüzün: *Flow of binary mixtures of equal-density granules in hoppers-size segregation, flowing density and discharge rates*. Chemical Engineering Science, 45(1):205–223, 1990.

[17] Ristow, G e HJ Herrmann: *Forces on the walls and stagnation zones in a hopper filled with granular material*. Physica A: Statistical Mechanics and its Applications, 213(4):474–481, 1995.

[18] Goda, TT e F Ebert: *Three-dimensional discrete element simulations in hoppers and silos*. Powder technology, 158(1):58–68, 2005.

[19] Baxter, GW, R Leone e RP Behringer: *Experimental test of time scales in flowing sand*. EPL (Europhysics Letters), 21(5):569, 1993.

[20] Behringer, RP e WG Baxter: *Pattern Formation and Complexity in Granular Flows*. Em Mehta, A (editor): *Granular Matter: An Interdisciplinary Approach*, páginas 85–119. Springer, New York.

[21] Gutiérrez, G, C Colonnello, P Boltenhagen, JR Darias, R Peralta-Fabi, F Brau e E Clément: *Silo Collapse under Granular Discharge*. Phys. Rev. Lett., 114:018001, Jan 2015. `http://link.aps.org/doi/10.1103/PhysRevLett.114.018001`.

[22] Jenike, AW: *Gravity flow of bulk solids*. Bulletin No. 108, Utah State University, 1961.

[23] Johanson, JR e AW Jenike: *Stress and velocity fields in gravity flow of bulk solids*. Bulletin of the University of Utah, 53(21), 1962.

[24] Jenike, AW: *Quantitative design of mass-flow bins*. Powder Technology, 1(4):237 – 244, 1967, ISSN 0032-5910. `http://www.sciencedirect.com/science/article/pii/0032591067800421`.

[25] Nguyen, TV, CE Brennen e RH Sabersky: *Funnel flow in hoppers*. Journal of Applied Mechanics, 47(4):729–735, 1980.

[26] González-Montellano, C, E Gallego, A Ramírez-Gómez e F Ayuga: *Three dimensional discrete element models for simulating the filling and emptying of silos: analysis of numerical results*. Computers & Chemical Engineering, 40:22–32, 2012.

[27] Medina, A, JA Cordova, E Luna e C Trevino: *Velocity field measurements in granular gravity flow in a near 2D silo*. Physics Letters A, 250(1):111–116, 1998.

[28] Kondic, L: *Simulations of two dimensional hopper flow*. Granular Matter, 16(2):235–242, 2014.

[29] Baran, O e L Kondic: *On velocity profiles and stresses in sheared and vibrated granular systems under variable gravity*. Physics of Fluids (1994-present), 18(12):121509, 2006.

[30] Ketterhagen, WR, JS Curtis, CR Wassgren e BC Hancock: *Predicting the flow mode from hoppers using the discrete element method*. Powder technology, 195(1):1–10, 2009.

[31] Nedderman, RM: *The measurement of the velocity profile in a granular material discharging from a conical hopper*. Chemical Engineering Science, 43(7):1507 – 1516, 1988, ISSN 0009-2509. http://www.sciencedirect.com/science/article/pii/000925098885142X.

[32] Sielamowicz, I e M Czech: *Analysis of the radial flow assumption in a converging model silo*. Biosystems engineering, 106(4):412–422, 2010.

[33] Rosato, A, KJ Strandburg, F Prinz e RH Swendsen: *Why the Brazil nuts are on top: Size segregation of particulate matter by shaking*. Physical Review Letters, 58(10):1038–1040, 1987.

[34] Rosato, A, F Prinz, KJ Standburg e R Swendsen: *Monte Carlo simulation of particulate matter segregation*. Powder Technology, 49(1):59–69, 1986.

[35] Haff, PK e BT Werner: *Computer simulation of the mechanical sorting of grains*. Powder Technology, 48(3):239–245, 1986.

[36] Duran, J, J Rajchenbach e E Clément: *Arching effect model for particle size segregation*. Physical review letters, 70(16):2431, 1993.

[37] Knight, JB, HM Jaeger e SR Nagel: *Vibration-induced size separation in granular media: The convection connection*. Physical review letters, 70(24):3728, 1993.

[38] Gallas, JAC, HJ Herrmann, T Pöschel e S Sokołowski: *Molecular dynamics simulation of size segregation in three dimensions*. Journal of Statistical Physics, 82(1):443–450, Jan 1996, ISSN 1572-9613. https://doi.org/10.1007/BF02189239.

[39] Pöschel, T e HJ Herrmann: *Size Segregation and Convection*. EPL (Europhysics Letters), 29(2):123, 1995. http://stacks.iop.org/0295-5075/29/i=2/a=003.

[40] Hong, DC, PV Quinn e S Luding: *Reverse Brazil nut problem: competition between percolation and condensation*. Physical Review Letters, 86(15):3423, 2001.

[41] Kudrolli, A: *Size separation in vibrated granular matter*. Reports on progress in physics, 67(3):209, 2004.

[42] Makse, HA, S Havlin e HE King, PR e Stanley: *Spontaneous stratification in granular mixtures*. Nature, 386:379–382, 1997.

[43] Grasselli, Y e HJ Herrmann: *Experimental study of granular stratification*. Granular Matter, 1(1):43–47, 1998.

[44] Peng, G e HJ Herrmann: *Density waves and 1/f density fluctuations in granular flow*. Physical Review E, 51(3):1745, 1995.

[45] Schick, KL e AA Verveen: *1/f noise with a low frequency white noise limit*. Nature, 251(5476):599–601, 1974.

[46] Muite, BK, SF Quinn, S Sundaresan e KK Rao: *Silo music and silo quake: granular flow-induced vibration*. Powder Technology, 145(3):190–202, 2004.

[47] Janssen, HA: *Versuche über Getreidedrack in Silozellen.* Zeitschrift des Vereines Deutscher Ingenieure, 39:1045–1049, 1895.

[48] Sperl, M: *Experiments on corn pressure in silo cells–translation and comment of Janssen's paper from 1895*. Granular Matter, 8(2):59–65, 2006.

[49] Šmíd, J e J Novosad: *Pressure distribution under heaped bulk solids*. Em *I. Chem. E. Symposium Series*, volume 63, 1981.

[50] Vanel, L, D Howell, D Clark, RP Behringer e E. Clément: *Memories in sand: Experimental tests of construction history on stress distributions under sandpiles*. Physical Review E, 60:5040, novembro 1999.

[51] Atman, APF, P Brunet, J Geng, G Reydellet, P Claudin, RP Behringer e E Clément: *From the stress response function (back) to the sand pile "dip"*. The European Physical Journal E: Soft Matter and Biological Physics, 17(1):93–100, 2005.

[52] Zuriguel, I e T Mullin: *The role of particle shape on the stress distribution in a sandpile*. Em *Proceedings of the Royal Society of London A: Mathematical, Physical and Engineering Sciences*, volume 464, páginas 99–116. The Royal Society, 2008.

[53] Liu, AJ e SR Nagel: *Nonlinear dynamics: Jamming is not just cool any more*. Nature, 396(6706):21–22, 1998.

[54] Cates, ME, JP Wittmer, J P Bouchaud e Ph Claudin: *Jamming, force chains, and fragile matter*. Physical Review Letters, 81(9):1841, 1998.

[55] To, Kiwing, Pik Yin Lai e HK Pak: *Jamming of granular flow in a two-dimensional hopper*. Physical Review Letters, 86(1):71, 2001.

[56] Mondal, S e MM Sharma: *Role of flying buttresses in the jamming of granular matter through multiple rectangular outlets*. Granular Matter, 16(1):125–132, 2014.

[57] Hidalgo, RC, C Lozano, I Zuriguel e A Garcimartín: *Force analysis of clogging arches in a silo*. Granular Matter, 15(6):841–848, 2013.

[58] Reynolds, Osborne: *LVII. On the dilatancy of media composed of rigid particles in contact. With experimental illustrations*. The London, Edinburgh, and Dublin Philosophical Magazine and Journal of Science, 20(127):469–481, 1885.

[59] *This file is licensed under the Creative Commons Attribution-Share Alike 3.0 Unported license.*, 2010. `http://commons.wikimedia.org/wiki/File:Reynold%27s_dilatancy.svg`.

[60] McNamara, S: *Turning Down the Volume on Granular Materials*. Physics, 9:35, 2016.

[61] Pöschel, T e T Schwager: *Computational Granular Dynamics*. Springer, 2005.

[62] Magalhães, CFM: *Simulação de materiais granulares*. Tese de Mestrado, Universidade Federal de Minas Gerais, setembro 2008.

[63] Magalhães, CFM: *Engarrafamento e segregação em empilhamentos abertos de grãos*. Tese de Doutoramento, Universidade Federal de Minas Gerais, abril 2013.

[64] Alder, BJ e TE Wainwright: *Studies in molecular dynamics. I. General method*. The Journal of Chemical Physics, 31(2):459–466, 1959.

[65] Cundall, PA: *A Computer Model for Simulating Progressive Large Scale Movements in Blocky Rock Systems*. Em *Proc. Int. Symp. Rock Fracture, ISRM*, páginas 2–8, Nancy (F), 1971.

[66] Leonardi, A, FK. Wittel, M Mendoza e HJ. Herrmann: *Coupled DEM-LBM method for the free-surface simulation of heterogeneous suspensions*. Computational Particle Mechanics, 1(1):3–13, May 2014, ISSN 2196-4386. https://doi.org/10.1007/s40571-014-0001-z.

[67] Leonardi, A, M Cabrera, FK Wittel, R Kaitna, M Mendoza, W Wu e HJ Herrmann: *Granular-front formation in free-surface flow of concentrated suspensions*. Phys. Rev. E, 92:052204, Nov 2015. https://link.aps.org/doi/10.1103/PhysRevE.92.052204.

[68] Leonardi, Al, FK Wittel, M Mendoza, R Vetter e HJ Herrmann: *Particle-Fluid-Structure Interaction for Debris Flow Impact on Flexible Barriers*. Computer-Aided Civil and Infrastructure Engineering, 31(5):323–333, 2016, ISSN 1467-8667. http://dx.doi.org/10.1111/mice.12165.

[69] Müller, P e T Pöschel: *Event-driven molecular dynamics of soft particles*. Physical Review E, 87(3):033301, 2013.

[70] Bird, GA: *Molecular gas dynamics*. NASA STI/Recon Technical Report A, 76, 1976.

[71] Hegselmann, R: *Cellular automata in the social sciences*. Em *Modelling and simulation in the social sciences from the philosophy of science point of view*, páginas 209–233. Springer, 1996.

[72] Peak, D, JD West, SM Messinger e KA Mott: *Evidence for complex, collective dynamics and emergent, distributed computation in plants*. Proceedings of the National Academy of Sciences, 101(4):918–922, 2004, ISSN 0027-8424. http://www.pnas.org/content/101/4/918.

[73] Aschenwald, J, S Fink e G Tappeiner: *Brave new modeling: Cellular automata and artificial neural networks for mastering complexity in economics*. Complexity, 7(1):39–47. https://onlinelibrary.wiley.com/doi/abs/10.1002/cplx.10011.

[74] Bak, P, C Tang e K Wiesenfeld: *Self-organized criticality: An explanation of the 1/f noise*. Physical Review Letters, 59(4):381, 1987.

[75] Allen, MP e DJ Tildesley: *Computer simulation of liquids*. Oxford university press, 2017.

[76] Gear, CW: *The numerical integration of ordinary differential equations of various orders*. Relatório Técnico, Argonne National Lab., Ill., 1966.

[77] Gear, CW: *Numerical Initial Value Problems in Ordinary Differential Equations*. Prentice-Hall, Englewood Cliffs, 1971.

[78] Hertz, H: *Über die Berührung fester elastischer Körper.* Journal für die reine und angewandte Mathematik, 94:156–171, 1882.

[79] Hertz, H, DE Jones e GA Schott: *English translation of Miscellaneous Papers*, 1896.

[80] Landau, L e EM Lifshitz: *Theory of Elasticity*. Pergamon Press, 2ª edição, 1970.

[81] Kruggel-Emden, H, E Simsek, S Rickelt, S Wirtz e V Scherer: *Review and extension of normal force models for the discrete element method*. Powder Technology, 171(3):157–173, 2007.

[82] Kuwabara, G e K Kono: *Restitution coefficient in a collision between two spheres*. Japanese journal of applied physics, 26(8R):1230, 1987.

[83] Brilliantov, NV, F Spahn, JM Hertzsch e T. Pöschel: *Model for collisions in granular gases*. Phys. Rev. E, 53(5):5382, 1996.

[84] Schäfer, J, S Dippel e DE Wolf: *Force schemes in simulations of granular materials*. Journal de physique I, 6(1):5–20, 1996.

[85] Cundall, PA e ODL Strack: *A discrete numerical model for granular assemblies*. Geotechnique, 29(1):47–65, 1979.

[86] Luding, S: *Molecular dynamics simulations of granular materials*. The physics of granular media, páginas 297–324, 2004.

[87] Mott, PH e CM Roland: *Limits to Poisson's ratio in isotropic materials*. Physical Review B, 80:132104, Oct 2009. `https://link.aps.org/doi/10.1103/PhysRevB.80.132104`.

[88] *Table for friction coefficientes from Engineer's Handbook website*, 2013. `http://www.engineershandbook.com/Tables/frictioncoefficients.htm`.

[89] Magalhães, FGR, APF Atman, JG Moreira e HJ Herrmann: *Analysis of the velocity field of granular hopper flow*. Granular Matter, 18(2):1–7, 2016.

[90] Martínez, L, R Andrade, EG Birgin e JM Martínez: *PACKMOL: a package for building initial configurations for molecular dynamics simulations*. Journal of computational chemistry, 30(13):2157–2164, 2009.

[91] Andrade, J, C Trevino e A Medina: *Experimental evidence of density fluctuations in two-dimensional bins*. Physics Letters A, 223(1-2):105–110, 1996.

[92] Howell, DW, RP Behringer e CT Veje: *Fluctuations in granular media*. Chaos: An Interdisciplinary Journal of Nonlinear Science, 9(3):559–572, 1999.

[93] Christensen, K e NR Moloney: *Complexity and criticality*, volume 1. Imperial College Press, 2005.

[94] Mandelbrot, BB e JR Wallis: *Robustness of the rescaled range R/S in the measurement of noncyclic long run statistical dependence*. Water Resources Research, 5(5):967–988, 1969.

[95] Feder, J: *Fractals*. Plenum Press, 1988.

[96] `http://plasma-gate.weizmann.ac.il/Grace/`.

[97] Kramar, M, A Goullet, L Kondic e K Mischaikow: *Persistence of force networks in compressed granular media*. Physical Review E, 87(4):042207, 2013.

[98] Radjai, F, DE Wolf, M Jean e J J Moreau: *Bimodal character of stress transmission in granular packings*. Physical Review Letters, 80(1):61, 1998.

[99] Majmudar, TS e RP Behringer: *Contact force measurements and stress-induced anisotropy in granular materials*. Nature, 435(7045):1079–1082, 2005.

[100] Zhang, HP e HA Makse: *Jamming transition in emulsions and granular materials*. Phys. Rev. E, 72:011301, Jul 2005. `https://link.aps.org/doi/10.1103/PhysRevE.72.011301`.

APPENDIX A – Paper

Granular Matter (2016) 18:33
DOI 10.1007/s10035-016-0636-y

ORIGINAL PAPER

Analysis of the velocity field of granular hopper flow

F. G. R. Magalhães[1,2,3] · **A. P. F. Atman**[4,5] · **J. G. Moreira**[1] · **H. J. Herrmann**[2,5,6]

Received: 23 July 2015 / Published online: 29 April 2016

Abstract We report the analysis of radial characteristics of the flow of granular material through a conical hopper. The discharge is simulated for various orifice sizes and hopper opening angles. Velocity profiles are measured along two radial lines from the hopper cone vertex: along the main axis of the cone and along its wall. An approximate power law dependence on the distance from the orifice is observed for both profiles, although differences between them can be noted. In order to quantify these differences, we propose a Local Mass Flow Index that is a promising tool in the direction of a more reliable classification of the flow regimes in hoppers.

Keywords Granular matter · Discrete element method · Velocity profile · Hopper flow

Electronic supplementary material The online version of this article (doi:10.1007/s10035-016-0636-y) contains supplementary material, which is available to authorized users.

✉ F. G. R. Magalhães
felipe@fisica.ufmg.br

[1] Departamento de Física, Universidade Federal de Minas Gerais, Caixa Postal 702, Belo Horizonte 30161-970, Brazil

[2] Computational Physics, IfB, ETH Zürich, Hönggerberg, 8093 Zurich, Switzerland

[3] Instituto de Ciências Exatas, Universidade Federal de Viçosa, Caixa Postal 22, Rio Paranaíba 38810-000, Brazil

[4] Departamento de Física e Matemática, Centro Federal de Educação Tecnológica de Minas Gerais, Belo Horizonte 30510-000, Brazil

[5] Instituto Nacional de Ciência e Tecnologia Sistemas Complexos, Belo Horizonte, Brazil

[6] Departamento de Física, Universidade Federal do Ceará, Fortaleza, Ceará 60451-970, Brazil

1 Introduction

The study of granular flows has attracted great interest from physicists and engineers due to its applicability and rich phenomenology [1–3], particularly due to the applications in the industrial and mining processes where it plays a crucial role [4]. Moreover, in the last decades, with the increasing computational performance of codes based on the discrete element method (DEM), there has been a new surge of interest on the subject with the possibility of studying large systems at the scale of real experiments. One of the oldest and most important cases of granular flow is the discharge of grains through a bottleneck. Efforts have been made to understand the multitude of features presented by this type of flow such as clogging [5–7], density fluctuations [8], segregation [9,10], strong fluctuations on the forces acting on silo walls [11,12] and the collapse of silos during discharge [13]. Another known property of granular discharges is that two distinct flow regimes can be observed—mass flow and funnel flow—, depending on the material properties of the grains and walls, and mostly on the hopper geometry (grain-wall friction, opening angle, orifice size, among others) [14–17]. In engineering applications, mass flow is usually desired, since it is the flow where grains leave the hopper in a "first-in, first-out" order. Oppositely, funnel flow is characterized by the presence of stagnation zones, so that part of the grains is slower or immobile and acts as a funnel next to the hopper walls. In some applications, such as typically the agricultural ones, the stagnant material may deteriorate causing direct loss of product as well as efficiency. Therefore, the better understanding of these phenomena, particularly the influence of the design of silos, can impact directly the industry of bulk solids.

The flow regime classification is often based on visualization of the steady state. Through the decades it has evolved

from the sole visual observation of stagnation zones on experiments [17] to the time averaged velocity spatial distributions, either by color scaled two-dimensional fields or profile curves along a certain linear path. Velocity profiles, particularly, are widely applied in the field of granular discharge flow [18–21]. The funnel flow regime is then recognized by the presence of stagnation zones in the velocity fields or a large difference between the velocity in the central region and that close to the walls. In order to quantify this difference, an index is defined [14,22], the Mass Flow Index (I_{MF}), corresponding to the ratio of the average particle velocity next to the hopper wall, v_{w}, to the average particle velocity at the hopper centerline, v_{c}, that is, $I_{\mathrm{MF}} = v_{\mathrm{w}}/v_{\mathrm{c}}$. It is defined such that if $I_{\mathrm{MF}} < 0.3$ the regime is funnel flow, and mass flow otherwise.

Ketterhagen et al. [22] used this index to create design charts for wedge shaped and conical hoppers, that is, they measured I_{MF} from simulations for different pairs of grain-wall friction and hopper wall angle and plotted them in a phase diagram to serve as a guideline for the designing of hoppers. For this, they averaged v_{w} and v_{c} over a large region spanning along the hopper walls and the centerline, respectively.

The velocity dependence on the vertical coordinate is usually assumed to be equal to that of an incompressible fluid [14,23]. In the case of an incompressible fluid flowing through a conical hopper with an angle α with the horizontal plane, we can easily obtain the velocity dependence on the vertical coordinate. Being the volume flow rate defined as $Q = Av$, where A is the cross sectional area and v is the velocity. The flow rate must be constant along the direction of the flow, provided that the density is homogeneous. Thus, consider a point at height z_o on the hopper opening, where $Q_o = A_o v_o$, and an arbitrary point at height z in the hopper, where $Q = Av$, then

$$\frac{Q}{Q_o} = \frac{Av}{A_o v_o} = \frac{\pi\,(z\tan\alpha)^2\,v}{\pi\,(z_o\tan\alpha)^2\,v_o} = 1$$

and, from that,

$$v = \left(\frac{z}{z_o}\right)^{-2} v_o. \tag{1}$$

Therefore, for an incompressible fluid, the velocity decays as a power law along z with exponent 2. However, if Eq. 1 holds for a granular discharge, the procedure used by Ketterhagen et al. [22] may lead to an I_{MF} value that is highly sensitive on position and size of the averaging region. This would cause their design charts to be applicable only if the same specifications were used. In fact, González-Montellano et al. [18] calculated the ratio of the wall and center velocities, but averaging them over small regions at a few different heights along a square cross-section silo with a hopper-bottom that also has square cross-section. Although the ratio is approximately equal to one all along the vertical silo, they observed that inside the hopper the ratio largely fluctuates reaching values below 0.3 at some points, even though they consider the discharge to be in the mass flow regime.

Granular flow may differ from incompressible fluids as there are voids and, therefore, density heterogeneities occur, even though each grain is roughly incompressible by itself. In fact, one can expect that a larger density would be observed at positions farther from the hopper outlet, where the velocity is smaller and the grains are in a densely packed structure, as compared to regions closer to the orifice, where the velocity is larger and grains are looser. As shown by Sielamowicz and Czech [24] in experiments discharging amaranth seeds through a two dimensional hopper, the assumption of an incompressible fluid is not always valid. They found discrepancies from the 2D equivalent to Eq. 1, specially, close to the outlet. Indeed, their flow regime was closer to funnel flow as there is the formation of a channel of flowing grains in the central region of the hopper, while the grains close to the walls of the hopper are stagnant. Also mixed flows may occur, where an upper section of the hopper is in mass flow regime whereas the bottom section is in funnel flow regime.

In order to contribute to this discussion, we present in this paper the velocity profiles along the centerline and along the walls of a conical hopper and we show that they behave roughly as power laws. Nevertheless, there are some differences between v_{c} and v_{w} profiles that carry information about the flow regime. We propose the analysis of the Local Mass Flow Index profile as a method capable of extracting that information in a clear way. Also, this method should be applicable independently of the validity of any assumption on the velocity radial dependence. Furthermore, we believe that the Local Mass Flow Index analysis may lead to a more precise definition of the flow regime boundaries.

2 Model

The microscopic model used for the grain interactions was described in details by Pöschel and Schwager [25]. A particle i, with radius R_i and at position $\vec{r}_i$, is in contact with a particle j if $\xi = \left[(R_i + R_j) - \left|\vec{r}_j - \vec{r}_i\right|\right] > 0$, where ξ is the overlap length. The normal force f_n is given by the Hertzian Law:

$$f_n = E_{\mathrm{eff}}\sqrt{R_{\mathrm{eff}}}\sqrt{\xi}\left(\xi + A\dot{\xi}\right), \tag{2}$$

where $\dot{\xi}$ is the normal relative velocity; $E_{\mathrm{eff}} = (E_i^{-1} + E_j^{-1})^{-1}$ is the effective elastic coefficient; $E_i = (4/3)[Y_i/(1-\nu_i^2)]$, where Y_i is the Young modulus and ν_i is the Poisson ratio of the material of particle i; $R_{\mathrm{eff}} = (R_i^{-1} + R_j^{-1})^{-1}$ is the effective radius and A is a normal damping constant

[26]. We also impose positive values for f_n, so that unphysical attractive forces are avoided. Therefore, the normal force vector is

$$\vec{F}_n = \max(0,\, f_n)\,\hat{e}_n, \tag{3}$$

where $\hat{e}_n = (\vec{r}_j - \vec{r}_i)/|\vec{r}_j - \vec{r}_i|$.

The tangential force is modeled in the spirit of Cundall and Strack's seminal paper [27] and implemented following description by Luding [28]. In the static regime the force is represented by an elastic term, analogously to a spring being attached to the points of the first contact of each of the particles surface, and a dissipative term,

$$\vec{f}_0 = -k_t\vec{\zeta} - \gamma_t\vec{v}_t \tag{4}$$

where $\vec{\zeta}$ is the spring displacement, k_t is the spring stiffness, γ_t is a tangential damping constant and $\vec{v}_t = \vec{v_{ij}} - \hat{e}_n(\hat{e}_n \cdot \vec{v_{ij}})$ is the tangential velocity. Only the tangential displacements are considered, so that $\vec{\zeta}$ and $\vec{v}_t$ are parallel to each other. If the tangential force is larger than the static friction limit, that is $f_0 > \mu_s f_n$, then the particles are in the dynamic regime, where the force is proportional to the normal force,

$$f_c = \mu_d f_n, \tag{5}$$

being μ_s and μ_d, respectively, the coefficient of static and of dynamic friction. Therefore, the tangential force is

$$\vec{F}_t = \hat{e}_t \cdot \begin{cases} f_0 & \text{if } f_0 \le \mu_s f_n \text{ (static regime)} \\ f_c & \text{if } f_0 > \mu_s f_n \text{ (dynamic regime)} \end{cases} \tag{6}$$

We use material parameters as follows: $E = 10^8$ Pa, which represents approximate values of $Y \sim 10^8$ Pa and $\nu \sim 0.1$, although Y and ν are not implemented directly; $\mu_s = 0.8$; $\mu_d = 0.6$; $k_t = 100$ N/m; $\gamma_t = 0.1$ kg/s; $A = 0.01$ s. The main reason for the choice of the value for k_t is guarantee that the particles were rarely at the dynamic friction regime and would roll rather than slip. Two friction coefficients where introduced following the method explained in details in reference [28]. This implies that the tangential force presents a discontinuity when two grains, that were in static contact, start to slip, as expected from an application of Coulomb's friction model, but no numerical instabilities were observed. In order to avoid crystallization, the radii of the spheres are randomly chosen from a uniform distribution from an interval of 5 % deviation around $R = 5$ mm. The density is 8×10^3 kg/m^3, therefore each grain weights about 4.2 g. Additionally to the contact forces, gravity acts on each particle and the acceleration of gravity in the simulations is set to $g = 10$ m/s^2 in the direction of $-\hat{z}$. The integration of Newton's equations of motion was performed using a fifth order Gear's predictor-corrector algorithm [25]. The time step was chosen as $\Delta t = 10^{-6}s$ so that it was at least two orders of magnitude smaller than the typical collision time, estimated for a collision velocity of 1 m/s and equations from Ref. [29].

In our simulations we use conical hoppers with different tilt angles $\alpha = 45°$, $60°$ or $75°$, measured from the horizontal plane, and study discharges of 20,000 grains for orifice diameters $D = 6R, 8R, 12R, 16R$ and $24R$. The walls are simulated by the force law given by Eqs. 3 and 6 where the overlap length ξ is that of the grain with the wall surface. Additionally, R_{eff} is chosen to be equal to the radius of the grain. The other material parameters are equal to those of collisions between grains.

The system is initialized by releasing the grains from a regular cubic lattice configuration inside the hopper with the grain centers separated typically by $3R$ or $4R$ with small random velocities while the hopper orifice is kept closed. The orifice is opened after a time of typically 0.5 s (5×10^5 time steps), what ensures that the velocity of the grains is much smaller than that they attain during the discharge. After that the discharge begins.

In order to maintain a stationary flow, grains that are more than one diameter below the outlet are reinserted at randomly chosen positions at the top surface of the material in the hopper, this procedure is carried out at regular intervals of 0.1 s (10^5 time steps). Thus, the number of particles inside the hopper is kept approximately constant all along the discharging process.

A snapshot of the system configuration can be seen in Fig. 1. The Cartesian and the spherical coordinate system are shown, for both cases the origin is chosen to coincide with the cone vertex. Also, the hopper angle with the horizontal plane, α, is defined.

3 Results and discussion

In order to visualize the steady-state flow, we create a velocity field. It is obtained by constructing a regular square grid over the plane (ρ, φ) representing by a color in each cell the modulus of the average velocity taken over grains inside that cell and the neighboring cells. Each cell is a ring of square section of sides equals to 0.002 m, however the averages are taken in a extended cell that includes the neighboring cells, that is the extended cell has sides of 0.006 m. This allows a finer picture, while it avoids an increase of statistical errors. The ring radius depends on the cell position on the r–z plane and uses the azimuthal symmetry and therefore the volumes are different. The grain is considered inside the cell if its center is in the extended cell. Additionally, the velocity is averaged over snapshots from the whole simulation, snapshots are taken every 0.005 s and the duration of each simulation is typically between 5 and 10 s. Some of

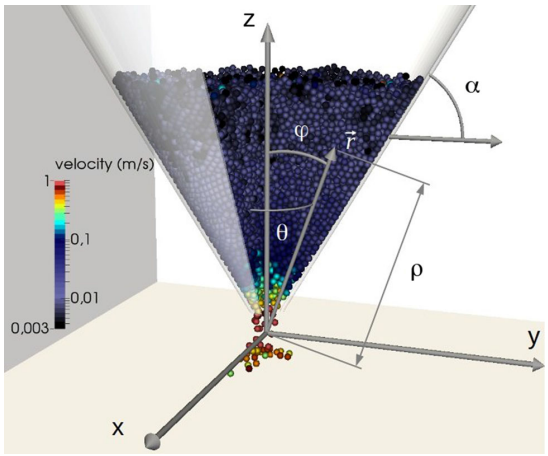

Fig. 1 Snapshot of hopper and flowing grains. Cartesian and spherical coordinates are shown, respectively, as (x, y, z) and (ρ, θ, φ). The parameters are $D = 8R$ and $\alpha = 60°$. The height of the packing is of approximately 40 grains or 0.4 m (color figure online)

those fields are shown in Fig. 2 for a few choices of orifice widths. Note that, by increasing the orifice size, the overall velocity increases. The iso-velocity curves, i.e. the borderline between two different color shades, are always crossing the entire horizontal extension of the hopper for orifice size $D = 8R$, while for $D = 16R$ there are enclosed regions close to the wall. Also, the general shape of these curves changes with the orifice size, being more horizontal for smaller orifice sizes and increasingly inclined for larger ones. This means that for the same distance from the vertex of the hopper the average velocity of the grains is larger at the center of the hopper than close to its walls.

The velocity field analysis may be useful to differentiate extreme states such as a fully developed funnel flow and a very typical mass flow. However, it is unable to quantify more subtle flow differences. Thus, in order to better characterize the flow, we contrast the two most different regions of the hopper, that is, we compute the velocity profile along ρ, the radial distance from the hopper cone vertex (Fig. 1), close to the wall of the hopper, $v_w(\rho)$, and along its central line, $v_c(\rho)$. These velocities are computed in a similar procedure to that of the velocity field. However, the sides of the square cells for the wall velocity are taken parallel and perpendicular to the walls of the hopper. Furthermore, we generalize the concept of Mass Flow Index to a Local Mass Flow Index profile, $I_{LMF}(\rho)$, similarly as in González-Montellano et al. [18]. It can be obtained directly from the velocity profiles as

$$I_{LMF}(\rho) = \frac{v_w(\rho)}{v_c(\rho)}.$$

We apply this analysis to data from simulations of discharges in hoppers of different orifice sizes, Fig. 3. The reader should note that the larger fluctuations seen in the center velocity profiles compared to the wall velocity are due to the smaller averaging volume, which is due to the azymuthal symmetry. In panel (a), a power law decay is observed for the velocity profiles along ρ. As discussed before, this behavior is not surprising, however, discrepancies between v_w and v_c are visible. We believe that these discrepancies carry information about the flow regime and should not be disregarded. For small orifice sizes, namely $D = 6R$ and $D = 8R$, the slope of the velocity along the center of the hopper appears to be larger than that along the walls, until they collapse into approximately the same curve further up in the hopper. On the other hand, for large orifice sizes, $D = 16R$ and $D = 24R$, there is a large gap between v_c and v_w all along ρ, and the slopes are very similar. Therefore, the gap is approximately maintained even for large ρ.

One could have analyzed this also through the I_{LMF} in Fig. 3b. The simulations with small opening diameters show I_{LMF} curves increasing with ρ, from $I_{LMF} \sim 0.8$ until they reach values close to unity, meaning the wall and center velocities are approaching identical values at higher positions. On the other hand, the curves for large opening widths

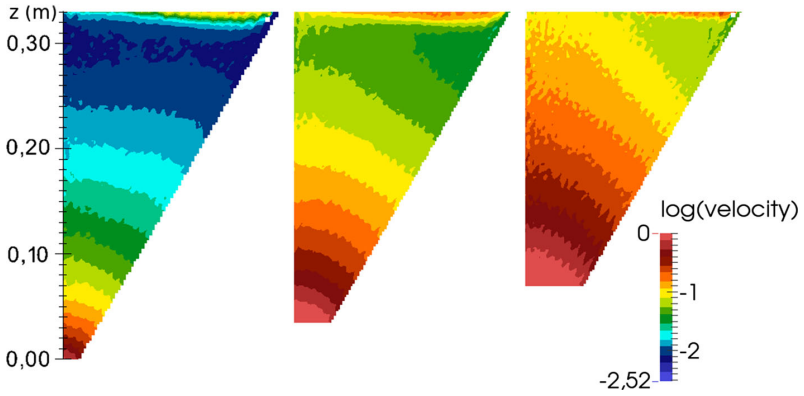

Fig. 2 Velocity field for $\alpha = 60°$ and $D = 8R$, $16R$ and $24R$, from *left* to *right*. *Color scale* is the modulus of the averaged velocity in units of log(m/s). Each cell is the rectangular section of a ring with sides equals to 0.002 m, however the average of the velocity is taken over grains inside that cell and the neighboring cells. The *top* of the hopper was cropped to avoid showing the free surface, where reinsertion dynamics dominates (color figure online)

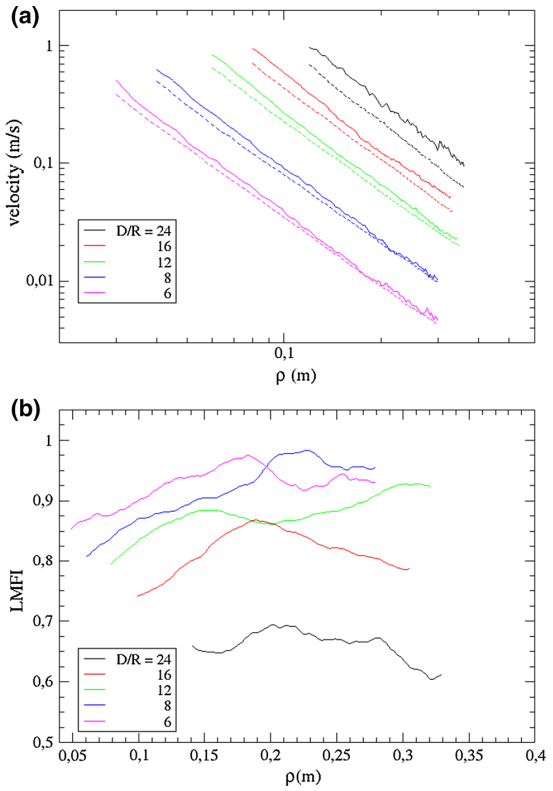

Fig. 3 Velocity profiles for center (*solid line*) and wall (*dashed line*) velocities in log-log scale (**a**) and Local Mass Flow Index (**b**) for different orifice diameters and $\alpha = 60°$. The profiles are power laws, but slightly different inclinations between v_w and v_c can be observed for some cases what causes the I_{LMF} to rise. The larger the orifice diameter the larger is the gap between center and wall velocities and consequently the lower is I_{LMF}. We estimate values of I_{MF} between 0.71 and 0.77 for these cases (color figure online)

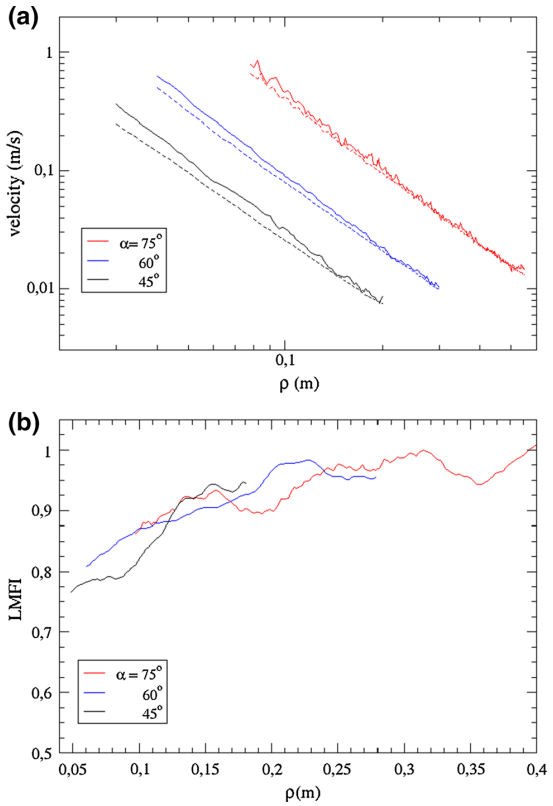

Fig. 4 Velocity profiles for center (*solid line*) and wall (*dashed line*) velocities in log-log scale (**a**) and Local Mass Flow Index (**b**) for different hopper angles and $D = 8R$. As in Fig. 3a, power law behavior is observed for the velocity profiles. Here, the differences between the center and wall velocities close to the outlet are larger for smaller θ, however, the difference vanishes for large ρ in all cases. This is represented in **b** by the low values of I_{LMF} for small ρ that then rise up to values close to unity. We estimate values of I_{MF} between 0.68 and 0.84 for these cases (color figure online)

fluctuate around much smaller values—$I_{LMF} \sim 0.65$ for $D = 24R$—, being a consequence of the approximately constant gap between v_c and v_w.

As we discussed in the Introduction, the commonly used Mass Flow Index is a unreliable tool as it may depend on the position and size of averaging window. The reason for this is made clear in Fig. 3a where the power law decaying velocity profile is confirmed. Moreover, the classification of the funnel flow regime as that in which $I_{MF} < 0.3$ is, then, questionable. Contrastingly, the Local Mass Flow Index, proposed here, is capable of distinguishing the typical mass flow behavior, such as the cases where $D = 6R, 8R$ and $12R$, from another regime where there are large differences between the center and wall velocities, even though stagnation zones are absent, cases $D = 16R$ and $24R$. This seems to be a precursor of the funnel flow regime where the wall velocity is much smaller than the center velocity all along the hopper.

By the usual definition of the Mass Flow Index, we estimate values close to $I_{MF} \sim 0,75$ for the five situations described in Fig. 3. Comparing these results to the I_{LMF}, we note that the I_{MF} values are quite close despite the differences of 30 % in the index that we propose. This occurs because the average of a quantity which varies with a power law, as the grain velocity, can induce mislead in the data interpretation.

Additionally, we present the analogous velocity profiles for hoppers of different opening angles, Fig. 4a. The same general behavior is observed, that is, a power law for both velocities. Differences between v_c and v_w are larger close to the outlet and decrease with increasing ρ. It is interesting to note that the I_{LMF} curves for each angle α, in Fig. 4b, are identical within the fluctuation range. This is a very interesting effect that we intend to investigate further for other open-

ing angles, but which will cost a considerable computational effort to be done. Comparing the I_{LMF} with the I_{MF} values, we can observe again that the latter is considerably less sensitive to the velocity fluctuations than the former. Again, we believe that this discrepancy is due to the averaging of a power law quantity, an issue subject to large fluctuations.

According to the literature [14,23], the velocity radial profiles should decay as a power law with exponent equals to 2, as calculated for an incompressible fluid in the Introduction of this paper. For all the cases, we obtained exponents around that value, the smallest value being 1.868(3) for $R = 12$ and $\alpha = 45°$ and the largest value being 2.176(5) for $R = 24$ and $\alpha = 60°$, both for the wall velocity profile. However, we observe in Figs. 3a and 4a that for the center velocity the slope of the profile varies along ρ. This is easily observed, for instance, for $R = 12$ and $\alpha = 45°$ (lower curves in Fig. 4a) where the center and wall velocity profiles are very close and approximately parallel for large ρ, but they separate close to the orifice. We believe this is an effect intrinsically related to the flow regime of the discharge and the local density heterogeneities. Moreover, the differences between the central and the wall velocity profiles can be highlighted by the Local Mass Flow Index. In most cases, the I_{LMF} shows an increase with ρ, presenting intermediate values, around 0.8, close to the outlet and rising further up until a value close to unity which means that v_{c} and v_{w} are equal. This effect is not observable by any other analysis. Also, for the case where the measured I_{LMF} is approximately constant, namely $D = 24R$ and $\alpha = 60°$, its value is relatively small, that is, close to the limit for funnel flow regime, even though it is expected to present mass flow.

In summary, our results show that the Local Mass Flow Index profile varies along ρ for many hopper angles and opening widths raising concerns over the characterization based solely on the Mass Flow Index, where this information is lost. The flow regime characterization is far too complex to be reduced to a single index. Nevertheless, the analysis of the I_{LMF} profiles was shown to be a very powerful tool to describe the more subtle aspects of the flow clearly. Although our simulations were limited to mass flow regime, we expect that more distinctive features will be observed for discharges in the funnel flow regime, what is part of our current investigations, which demands considerable larger CPU times.

4 Conclusions

We have investigated the influence of the orifice size and hopper opening angle on the velocity fields and profiles of spherical grains flowing through a conical hopper.

The fields show the presence of low velocity zones close to the walls of the hopper, only observed in systems with large outlet sizes. They seem to be precursors of stagnation zones that appear in fully developed funnel flow. Also,for larger orifice widths as compared to the smaller ones studied, the iso-velocity curves present a larger inclination, that is, the average velocity at the center of the hopper is larger than the velocity close to its wall for the same distance from the hopper vertex. Although these differences do not characterize different flow regimes, they show that there is a spectrum of behaviors for each flow regime.

The velocity profiles along the axis of the hopper and close to the walls were studied, as well as their ratio, the I_{LMF} profile. Both velocity profiles show approximately a power law dependence with the distance from the vertex of the hopper for the considered cases. In hoppers with large orifice widths, there is an upshift of the velocity profile along the center of the hopper as compared to that close to the walls, but the slopes are roughly the same. This is accompanied by a I_{LMF} that fluctuates around a certain value that can be as low as 0.65 for the largest orifice width analyzed. On the other hand, for small outlets, the difference between the profiles decreases with the distance from the opening. This decrease is clearer when the angle of the hopper is changed. The smaller the angle of the walls of the hopper with the horizontal plane, the larger the slope of the central velocity profile compared to the wall velocity profile. In all cases, the velocity profiles do not cross each other, so that, for a distance farther from the orifice, the difference of the slopes becomes negligible. This decrease in difference between the velocity profiles is seen as an increase of I_{LMF}. The I_{LMF} stabilizes with values close to one in the regions where the velocity profiles collapse.

We believe that the presented comparative analysis of the velocity profile at the center and close to the walls of the hopper accompanied by the I_{LMF} profile is a promising tool for the classification the granular flow regimes. It provides a broader and more intelligible picture of the flow state than the techniques currently applied in the field and it lacks the set-up sensitivity of other methods. We are currently working on applying this analysis to different silo geometries, such as flat and conical bottom cylindrical silos. In those cases a fully developed funnel flow is more easily accessible and, for that regime, we expect the I_{LMF} analysis to present some new insights.

Acknowledgments FGRM would like to thank Alessandro Leonardi for helpful discussions, as well as the whole Computational Physics Group at ETH Zürich for the hospitality and resources.

Compliance with ethical standards

Conflict of interest This project was partially funded by Grant No. FP7-319968-FlowCCS of the European Research Council (ERC) Advanced Grant and Brazilian agencies CAPES, CNPq and Ciências sem Fronteiras. The authors declare that they have no conflict of interest.

References

1. Duran, J.: Sands, Powders, and Grains, vol. 12. Springer, New York (2000)
2. Campbell, C.S.: Granular material flows—an overview. Powder Technol. **162**(3), 208–229 (2006)
3. Herrmann, H.J.: Grains of understanding. Phys. World **10**(11), 31–34 (1997)
4. Cleary, P.W., Sawley, M.L.: DEM modelling of industrial granular flows: 3D case studies and the effect of particle shape on hopper discharge. Appl. Math. Model. **26**(2), 89–111 (2002)
5. Zuriguel, I.: Clogging of granular materials in bottlenecks. Pap. Phys. **6**, 060014 (2014)
6. Janda, A., Zuriguel, I., Garcimartín, A., Pugnaloni, L.A., Maza, D.: Jamming and critical outlet size in the discharge of a two-dimensional silo. Europhys. Lett. **84**(4), 44002 (2008)
7. Magalhães, C.F.M., Atman, A.P.F., Combe, G., Moreira, J.G.: Jamming transition in a two-dimensional open granular pile with rolling resistance. Pap. Phys. **6**, 060007 (2014)
8. Ristow, G., Herrmann, H.J.: Density patterns in two-dimensional hoppers. Phys. Rev. E **50**, R5(R) (1994)
9. Artega, P., Tüzün, U.: Flow of binary mixtures of equal-density granules in hoppers-size segregation, flowing density and discharge rates. Chem. Eng. Sci. **45**(1), 205–223 (1990)
10. Magalhães, C.F.M., Moreira, J.G., Atman, A.P.F.: Segregation in arch formation. Eur. Phys. J. E Soft Matter Biol. Phys. **35**(5), 1–5 (2012)
11. Ristow, G.H., Herrmann, H.J.: Forces on the walls and stagnation zones in a hopper filled with granular material. Phys. A Stat. Mech. Appl. **213**(4), 474–481 (1995)
12. Goda, T.T., Ebert, F.: Three-dimensional discrete element simulations in hoppers and silos. Powder Technol. **158**(1), 58–68 (2005)
13. Gutiérrez, G., Colonnello, C., Boltenhagen, P., Darias, R., Peralta-Fabi, J.R., Brau, F., Clément, E.: Silo collapse under granular discharge. Phys. Rev. Lett. **114**, 018001 (2015)
14. Jenike, A.W.: Gravity flow of bulk solids. Bulletin No. 108, Utah State University (1961)
15. Johanson, J.R., Jenike, A.W.: Stress and velocity fields in gravity flow of bulk solids. Bull. Univ. Utah **53**(21) (1962)
16. Jenike, A.W.: Quantitative design of mass-flow bins. Powder Technol. **1**(4), 237–244 (1967)
17. Nguyen, T.V., Brennen, C.E., Sabersky, R.H.: Funnel flow in hoppers. J. Appl. Mech. **47**(4), 729–735 (1980)
18. González-Montellano, C., Gallego, E., Ramírez-Gómez, A., Ayuga, F.: Three dimensional discrete element models for simulating the filling and emptying of silos: analysis of numerical results. Comput. Chem. Eng. **40**, 22–32 (2012)
19. Medina, A., Cordova, J.A., Luna, E., Trevino, C.: Velocity field measurements in granular gravity flow in a near 2d silo. Phys. Lett. A **250**(1), 111–116 (1998)
20. Kondic, L.: Simulations of two dimensional hopper flow. Granul. Matter **16**(2), 235–242 (2014)
21. Baran, O., Kondic, L.: On velocity profiles and stresses in sheared and vibrated granular systems under variable gravity. Phys. Fluids (1994-present) **18**(12), 121509 (2006)
22. Ketterhagen, W.R., Curtis, J.S., Wassgren, C.R., Hancock, B.C.: Predicting the flow mode from hoppers using the discrete element method. Powder Technol. **195**(1), 1–10 (2009)
23. Nedderman, R.M.: The measurement of the velocity profile in a granular material discharging from a conical hopper. Chem. Eng. Sci. **43**(7), 1507–1516 (1988)
24. Sielamowicz, I., Czech, M.: Analysis of the radial flow assumption in a converging model silo. Biosyst. Eng. **106**(4), 412–422 (2010)
25. Pöschel, T., Schwager, T.: Computational Granular Dynamics. Springer, Berlin (2005)
26. Brilliantov, N.V., Spahn, F., Hertzsch, J.-M., Pöschel, T.: Model for collisions in granular gases. Phys. Rev. E **53**(5), 5382 (1996)
27. Cundall, P.A., Strack, O.D.L.: A discrete numerical model for granular assemblies. Geotechnique **29**(1), 47–65 (1979)
28. Luding, S.: Molecular dynamics simulations of granular materials. In: Hinrichsen, H., Wolf, D.E. (eds.) The Physics of Granular Media, pp 297–324. (2004). doi:10.1002/352760362X.ch13
29. Schäfer, J., Dippel, S., Wolf, D.E.: Force schemes in simulations of granular materials. J. Phys. I **6**(1), 5–20 (1996)